NEUROSCIENCE

Cross-talk between GABAergic postsynapse and microglia regulate synapse loss after brain ischemia

Teresa Cramer[1]†, Raminder Gill[2]†, Zahra S. Thirouin[3]†‡, Markus Vaas[4]†, Suchita Sampath[1], Fanny Martineau[5], Sara B. Noya[1], Patrizia Panzanelli[6], Tania J. J. Sudharshan[1], David Colameo[1], Philip K.-Y. Chang[2], Pei You Wu[2], Roy Shi[2], Philip A. Barker[7], Steven A. Brown[1], Rosa C. Paolicelli[5], Jan Klohs[8], Rebecca Anne McKinney[2]*‡, Shiva K. Tyagarajan[1,2]*‡

Microglia interact with neurons to facilitate synapse plasticity; however, signal(s) contributing to microglia activation for synapse elimination in pathology are not fully understood. Here, using in vitro organotypic hippocampal slice cultures and transient middle cerebral artery occlusion (MCAO) in genetically engineered mice in vivo, we report that at 24 hours after ischemia, microglia release brain-derived neurotrophic factor (BDNF) to downregulate glutamatergic and GABAergic synapses within the peri-infarct area. Analysis of the cornu ammonis 1 (CA1) in vitro shows that proBDNF and mBDNF downregulate glutamatergic dendritic spines and gephyrin scaffold stability through p75 neurotrophin receptor (p75^{NTR}) and tropomyosin receptor kinase B (TrkB) receptors, respectively. After MCAO, we report that in the peri-infarct area and in the corresponding contralateral hemisphere, similar neuroplasticity occurs through microglia activation and gephyrin phosphorylation at serine-268 and serine-270 in vivo. Targeted deletion of the *Bdnf* gene in microglia or *Gphn*S268A/S270A (phospho-null) point mutations protects against ischemic brain damage, neuroinflammation, and synapse downregulation after MCAO.

INTRODUCTION

Ischemic stroke is a leading cause of death and long-term disability worldwide. The annual mortality rate of 5.5 million is further compounded by high morbidity as up to 50% survivors are chronically disabled (*1*). Therapeutic approaches to central nervous system (CNS) ischemia developed in the laboratory have focused on mechanisms contributing to ischemic damage, namely, excitotoxicity, oxidative stress, and inflammation (*2*, *3*). Unfortunately, to date, clinical trials targeting glutamate receptors, γ-aminobutyric acid (GABA) receptors, calcium channels, sodium channels, and free radicals have all failed. The lack of treatment options is directly related to our poor understanding of the possible mechanisms underlying the disease. As the brain has developed inherent mechanism(s) for self-preservation, gaining insights into these protective measures may thus provide a way forward to counteract ischemic brain injury.

Typically, rapid cell death occurs in the ischemic core, but neurons in the peri-infarct area, a region with constrained blood flow and partially preserved energy metabolism, survive. Within the peri-infarct, the propagating neuronal depolarization in combination with impairment of glia function causes an increased extracellular concentration of ions and neurotransmitters, resulting in neuronal functional perturbations (*4*). This is accompanied by reductions in both excitatory dendritic spines (*5*) and GABAergic synapses (*6*). The neurotrophin brain-derived neurotrophic factor (BDNF) can decrease cell death and ischemic core volume, leading to improvement of neurological outcome after experimental stroke either upon overexpression in vivo using genetic methods (*7*) or upon exogenous application (*8*). Correspondingly, inhibition of BDNF exacerbates ischemic damage.

Under physiological conditions, glutamatergic neurotransmission induces BDNF expression. BDNF is expressed as a proprotein, proBDNF, and is subsequently processed to its mature form, mBDNF. proBDNF preferentially binds to the low-affinity nerve growth factor receptor p75^{NTR} and negatively regulates dendritic spine stability through Rho guanosine triphosphatases, Rho/Rac1 activation (*9*). mBDNF signals through the neurotrophin receptor tyrosine kinase B (TrkB) to enhance excitatory neurotransmission (*10*). mBDNF can also bind to p75^{NTR} receptors, albeit with much lower affinity (*11*). At inhibitory GABAergic synapses, mBDNF induces the internalization of GABA type A (GABA$_A$) receptors and down-regulation of the main inhibitory synapse scaffolding protein gephyrin (*12*), thereby reducing GABAergic transmission in principal cells.

Inflammatory pathways are also activated after ischemia that subsequently recruit leukocytes to the injured area of the brain (*13*). Immune cells contribute to both neuroprotection and programmed cell death, suggesting that the temporal window of inflammation might determine cell survival or death. The immune response signaling events must be counteracted to mitigate tissue damage

[1]Institute of Pharmacology and Toxicology, University of Zurich, Winterthurerstrasse 190, CH 8057 Zürich, Switzerland. [2]Department of Pharmacology and Therapeutics, McGill University, 3649 Prom. Sir-William-Osler, Montreal, QC H3G 0B1, Canada. [3]Research Institute of the McGill University Health Centre, 1650 Cedar Avenue, Montreal, QC H3G1A4, Canada. [4]Clinical Trials Center, University Hospital Zurich, Rämistrasse 100/MOU2, CH 8044 Zürich, Switzerland. [5]Department of Biomedical Sciences, University of Lausanne, Rue du Bugnon 7, CH 1005 Lausanne, Switzerland. [6]Department of Neuroscience Rita Levi Montalcini, University of Turin, Turin, Italy. [7]Department of Biology, University of British Columbia, 3187 University Way, ASC 413, Kelowna, BC V1V 1V7, Canada. [8]Institute for Biomedical Engineering, University of Zurich and ETH Zurich, Wolfgang-Pauli-Strasse 27, CH 8093 Zürich, Switzerland.
*Corresponding author. Email: tyagarajan@pharma.uzh.ch (S.K.T.); anne.mckinney@mcgill.ca (R.A.M.)
†These authors contributed equally to this work and share first authorship.
‡These authors contributed equally as senior authors.

and reestablish homeostasis. Microglia, the resident immune cells in the CNS, are the primary responders during defense. They clear cellular debris as part of the tissue repair and wound healing processes (14, 15). In recent years, microglia have also been shown to play an essential role in synapse pruning during postnatal brain development (16). Microglia activation can be triggered by acute insult, causing process elongation and increased expression of marker proteins such as ionized calcium–binding adaptor protein-1 (IBA1) and CD11b (17). Microglial activation can protect the brain, albeit the precise cellular and molecular mechanisms for microglia influenced neuroprotection remain unclear. Microglia processes can directly sense synaptic activity (18) and can regulate neuronal calcium load and functional connectivity through neuronal mitochondrial function and P2Y12 receptor activation on contacting microglia (19). Subsequent inflammation induced by lipopolysaccharide (LPS) activates downstream calcium/calmodulin-dependent kinase IV, and cyclic adenosine 5′-monophosphate response element (CRE)–binding protein (CREB) phosphorylation and BDNF protein increase facilitate neuron survival after cortical injury (20).

It has been reported that BDNF administered either intravenously (8), with viral vectors (7), or by addition of the bioactive high-affinity TrkB agonist, 7,8-dihydroxyflavone, can protect neurons from apoptosis and decrease infarct volumes in animal models of stroke (21). These findings suggest that elevated BDNF is beneficial for recovery after stroke. However, the mechanisms underlying the beneficial effect of BDNF after ischemia remain unclear. Here, we set out to assess the physiological mechanisms that are triggered upon ischemic brain damage to enable tissue repair and neural network reorganization. Using organotypic hippocampal slice cultures and the oxygen-glucose deprivation (OGD) cellular model of ischemia, we report that, within the first 90 min after ischemia, proBDNF via p75^{NTR} disrupts glutamatergic, and mBDNF via TrkB disrupts GABAergic neurotransmission. We found that extracellular signal–regulated kinase 1/2 (ERK1/2) and glycogen synthase kinase 3β (GSK3β) pathways downstream of TrkB phosphorylate gephyrin at Ser^{268} and Ser^{270} residues, resulting in GABAergic synapse loss. Using transient middle cerebral artery occlusion (MCAO) in wild-type (WT) and genetically engineered mice, we uncover a central role for BDNF derived from microglia in influencing gephyrin phosphorylation downstream of TrkB receptor signaling. Using pharmacological depletion of microglia, CRISPR-Cas9–generated *Gphn*S268A/S270A mutant mouse, and *Bdnf* gene deletion from microglia, we consistently demonstrate reduced microglial activation and enhanced synapse preservation at 24 hours after MCAO. Collectively, these observations unravel microglia-derived BDNF as the signal transducer linking microglia and neurons, to activate ERK1/2 and GSK3β pathways to influence glutamatergic and GABAergic synapse integrity through gephyrin phosphorylation.

RESULTS
OGD causes glutamatergic and GABAergic synapse down-regulation
To understand the mechanisms of BDNF action in ischemia, we started with an in vitro model of ischemia, OGD, in organotypic hippocampal slice cultures obtained from transgenic mice that express myristoylated enhanced green fluorescent protein (GFP) in a subset of CA1 pyramidal neurons and studied synaptic changes in the CA1 area after OGD (4 min) and recovery at 90 min and

24 hours. First, we confirmed that we had induced hypoxia with OGD by measuring hypoxia-inducible factor 1α (HIF1α) expression (22) and found 1.5-fold increase in HIF1α expression in area CA1 90 min after OGD (fig. S1, A and A′). We then determined glutamatergic synapse alterations after OGD by measuring changes in dendritic spines. We observed an overall significant reduction in spine density on CA1 pyramidal neurons at both 90 min and 24 hours following OGD compared to control cultures (Fig. 1, A and B, and fig. S1B). The mushroom and long-thin subtype of spines were particularly affected (Fig. 1B).

Next, we evaluated OGD-induced changes at GABAergic synapses in area CA1 at 90 min and 24 hours following OGD. We immunolabeled inhibitory presynaptic vesicular GABA transporter (VGAT) and postsynaptic inhibitory scaffolding protein gephyrin. We found a significant overall down-regulation in gephyrin cluster density 90 min following OGD compared to control (Fig. 1, C to E) in the stratum radiatum. However, after 24 hours, gephyrin cluster density remained significantly reduced, while cluster volume had recovered to baseline (fig. S1, B′ and B″) similar to untreated cells.

To determine whether these morphological changes were accompanied by a functional deficit, we recorded AMPA-mediated miniature excitatory postsynaptic currents (mEPSCs) from CA1 pyramidal neurons within 24 hours after OGD (Fig. 1, F and F′). We found that the input resistance and resting membrane potential of CA1 hippocampal pyramidal cells in OGD and sister untreated cells were similar, suggesting that OGD does not affect receptor open probability or intracellular chloride concentration. However, we found a significant decrease in the mEPSC amplitude in OGD-treated slices compared to control (Fig. 1F). Similarly, the interevent interval (IEI) of mEPSC of OGD cells was increased compared to control (Fig. 1F′). Together, dendritic spine loss is mirrored by functional loss of excitatory synapses 24 hours after OGD. Subsequently, to determine whether inhibitory circuitry was also affected, we recorded GABA$_A$-mediated miniature inhibitory postsynaptic current (mIPSC) within 24 hours of OGD induction. mIPSC analysis showed no observable changes in the amplitude of mIPSC after OGD compared to control slices (Fig. 1G). However, a significant increase in the IEI in OGD-treated slices was observed (Fig. 1G′). These functional data recapitulate the morphological observations that inhibitory synapse loss after OGD does not recover, but total GABA$_A$ receptors (GABA$_A$Rs) at synaptic sites within the existing synapses recover at 24 hours after OGD.

Scavenging BDNF after OGD using TrkB-Fc rescues OGD-induced synapse deficit
As BDNF is up-regulated after ischemia (23, 24), we assessed whether BDNF signaling contributed to synapse loss on CA1 pyramidal neurons after OGD. We scavenged proBDNF and mBDNF using chimeric TrkB-Fc (10 μg/ml) and exposed organotypic hippocampal slices to 4-min OGD. Dendritic spine quantification in CA1 pyramidal neurons showed prevention of total spine density loss caused by OGD in TrkB-Fc–treated cultures in comparison to untreated cultures (Fig. 2, A and B). Specifically, the OGD-induced decrease in mushroom and long-thin subtype of dendritic spines was prevented by TrkB-Fc (Fig. 2, A and B). We next assessed whether TrkB-Fc treatment also protects GABAergic synapses. We found that postsynaptic gephyrin clustering was protected by TrkB-Fc in OGD-treated cultures (Fig. 2, C to E). Using near super-resolution microscopy, we evaluated TrkB-Fc localization at glutamatergic
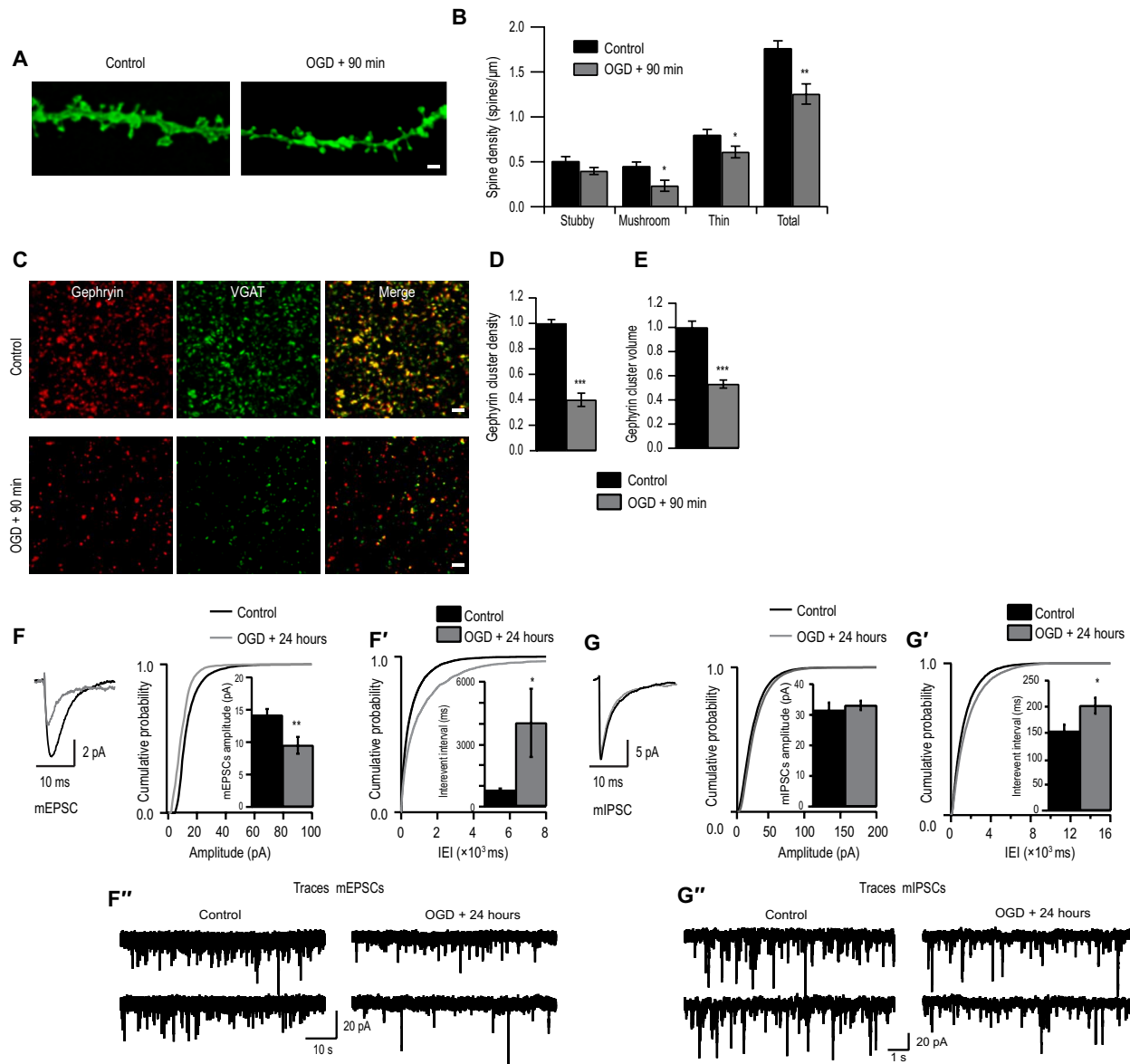
Fig. 1. OGD induces morphological and functional deficits in excitatory synapses. (**A**) Example tertiary dendrites from CA1 pyramidal neurons expressing myristoylated–enhanced GFP (eGFP) in control versus 90 min after OGD organotypic hippocampal cultures. Scale bar, 2 µm. (**B**) Quantification of dendritic spines categorized into stubby, mushroom, and long-thin subtypes (*$P < 0.05$ and **$P < 0.01$, two-tailed independent Student's t test). Total spine density (spines per micrometer of dendrite): Control, 1.76 ± 0.08 ($n = 8$); OGD, 1.25 ± 0.11 ($n = 8$). (**C**) Example images of maximum intensity projections of area CA1 immunostained for gephyrin and VGAT in control cultures versus 90 min following OGD. Scale bars, 2 µm. (**D**) Quantification of number of gephyrin clusters per confocal stack (consisting of five 512 pixel–by–512 pixel z planes each; ***$P < 0.001$, two-tailed independent Student's t test; gephyrin cluster values were normalized to control). Mean number [arbitrary units (A.U.)]: Control, 1.00 ± 0.03 ($n = 10$ slices); OGD, 0.40 ± 0.05 ($n = 10$ slices). (**E**) Quantification of the total volume of gephyrin cluster (***$P < 0.001$, two-tailed independent Student's t test). Mean volume (A.U.): Control, 1.00 ± 0.05; OGD, 0.53 ± 0.03. Data are shown as means $\pm$ SD ($n = 30$ cells). (**F**) Cumulative probability histogram and means $\pm$ SEM amplitude (**$P < 0.01$, Kolmogorov-Smirnov test). (**F'**) Cumulative probability histogram and means $\pm$ SEM for IEIs of mEPSCs (*$P < 0.05$, Kolmogorov-Smirnov test). (**F"**) Sample mEPSC traces from control cells and OGD cells. (**G**) Cumulative probability histogram and means $\pm$ SEM amplitude of mIPSCs ($P > 0.05$, Kolmogorov-Smirnov test). (**G'**) Cumulative probability histogram and means $\pm$ SEM for IEIs of mIPSCs (*$P < 0.05$, Kolmogorov-Smirnov test). (**G"**) Sample mEPSC traces from control cells and OGD cells. Data are shown as means $\pm$ SD.

and GABAergic synapses. For this, we treated primary hippocampal neurons (15 days old) with TrkB-Fc (10 µg/ml) and costained post-synaptic density 95 (PSD95) or gephyrin. Quantification shows 64% colocalization with PSD95 and 30% colocalization with gephyrin.

To determine whether morphological synapse protection is recapitulated functionally, we recorded excitatory AMPA-mediated

mEPSC from CA1 pyramidal neurons from all groups. We found that the OGD-induced reduction of mEPSC amplitudes 24 hours following OGD was prevented by TrkB-Fc treatment, being comparable to treated and untreated controls (Fig. 2F and fig. S1, C to C"). Similarly, the increase in IEI was also prevented by TrkB-Fc treatment as seen 24 hours after the induction of OGD, with values similar to treated and untreated
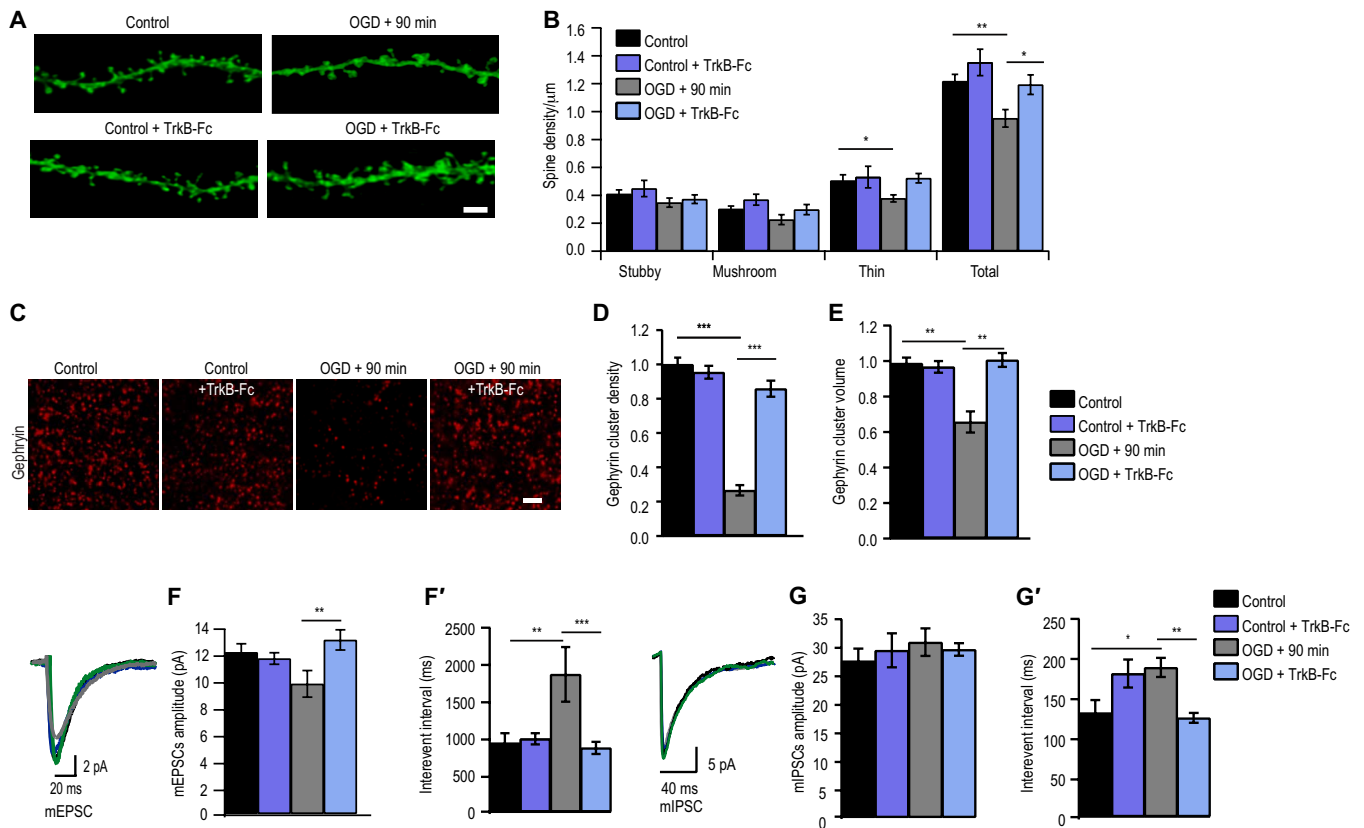
Fig. 2. Scavenging BDNF rescues OGD-induced synapse deficits. (**A**) Example dendrites from CA1 neurons expressing myristoylated-eGFP with and without TrkB-fc treatment. Scale bar, 2 μm. (**B**) Quantification of dendritic spines [*$P < 0.05$, **$P < 0.01$, two-way analysis of variance (ANOVA) with Bonferroni multiple comparison test]. Total spine density (spines per micrometer of dendrite): Control, 1.22 ± 0.05 ($n = 16$); Control + TrkB-Fc, 1.40 ± 0.10 ($n = 12$); OGD, 0.95 ± 0.06 ($n = 12$); OGD + TrkB-Fc, 1.19 ± 0.07 ($n = 14$). (**C**) Example images of maximum intensity projections of organotypic hippocampal slices immunostained for gephyrin with and without TrkB-Fc treatment. Scale bar, 2 μm. (**D**) Quantification of number of gephyrin puncta per confocal stack (consisting of five 512 pixel–by–512 pixel z planes each; ***$P < 0.001$, two-way ANOVA with Bonferroni multiple comparison test; all gephyrin values were normalized to control). Mean number (A.U.): Control, 1.00 ± 0.04 ($n = 15$); Control + TrkB-Fc, 0.95 ± 0.04 ($n = 9$ slices); OGD, 0.27 ± 0.03 ($n = 13$); OGD+TrkB-Fc, 0.86 ± 0.05 ($n = 13$). (**E**) Quantification of gephyrin puncta volume (**$P < 0.01$, two-way ANOVA with Bonferroni multiple comparison test). Mean volume (A.U.): Control, 1.00 ± 0.03; Control + TrkB-Fc, 0.98 ± 0.03; OGD, 0.67 ± 0.06; OGD + TrkB-Fc, 1.02 ± 0.04. Data are shown as means $\pm$ SD ($n = 30$ cells). (**F**) Cumulative probability histogram of mean amplitude (**$P < 0.01$, two-way ANOVA with Bonferroni multiple comparison test). (**F′**) Cumulative probability histogram for IEIs of mEPSCs (**$P < 0.01$, ***$P < 0.001$, two-way ANOVA with Bonferroni multiple comparison test). (**G**) Cumulative probability histogram of mean amplitude of mIPSCs ($P < 0.05$ two-way ANOVA with Bonferroni multiple comparison test). (**G′**) Cumulative probability histogram for IEIs of mIPSCs (*$P < 0.05$, **$P < 0.01$, two-way ANOVA with Bonferroni multiple comparison test). Data are shown as means $\pm$ SD.

control slices (Fig. 2F′ and fig. S1C′), indicating that the reduced occurrence of mEPSC after OGD was due to BDNF signaling.

To test whether TrkB-Fc also prevented changes in inhibitory transmission, we recorded GABA$_A$-mediated mIPSC from CA1 pyramidal neurons from all groups. We found that mIPSC amplitudes were comparable in all groups (Fig. 2, G and G′, and fig. S1, D to D″). The previously observed increase in IEI caused by OGD was prevented with TrkB-Fc treatment to control levels (Fig. 2G′ and fig. S1D′). Together, this suggests that the OGD-induced decrease in glutamatergic and GABAergic synapse loss is likely due to BDNF signaling.

proBDNF and mBDNF signal via p75^NTR and TrkB receptors to induce glutamatergic and GABAergic synapse loss, respectively, after ischemia

Next, we investigated the molecular pathways involving BDNF-mediated synapse loss at 90 min after OGD in organotypic hippocampal slice cultures. To specifically investigate the contribution of proBDNF on OGD-induced dendritic spine loss, we used blocking antibodies to either inhibit proBDNF or p75^{NTR}. Pretreatment of OGD slices with either anti-proBDNF or anti-p75^{NTR} antibodies prevented OGD-induced dendritic spine loss (Fig. 3, A to C; $P = 0.37$). In addition, treatment of OGD slices with anti-proBDNF or anti-p75^{NTR} antibody did not prevent gephyrin cluster loss after OGD (Fig. 3D; $P = 0.52$). These findings indicate that proBDNF signaling through p75^{NTR} to specifically induce excitatory synapses loss following OGD.

We next investigated the role of mBDNF in OGD-induced synapse loss. For this, we pretreated cultures with anti-mBDNF (N-9, a function blocking antibody) before OGD and then quantified the dendritic spines; control sister cultures were processed simultaneously with and without anti-mBDNF treatment. The data revealed a significant down-regulation of total dendritic spines in both OGD and anti-mBDNF pretreated OGD slices, compared to control and cultures pretreated with anti-mBDNF (Fig. 3, E and F). Similar to our earlier observations, only the mushroom and long-thin subtype of dendritic spines were down-regulated 90 min following OGD with or without anti-mBDNF treatment (Fig. 3F). These data
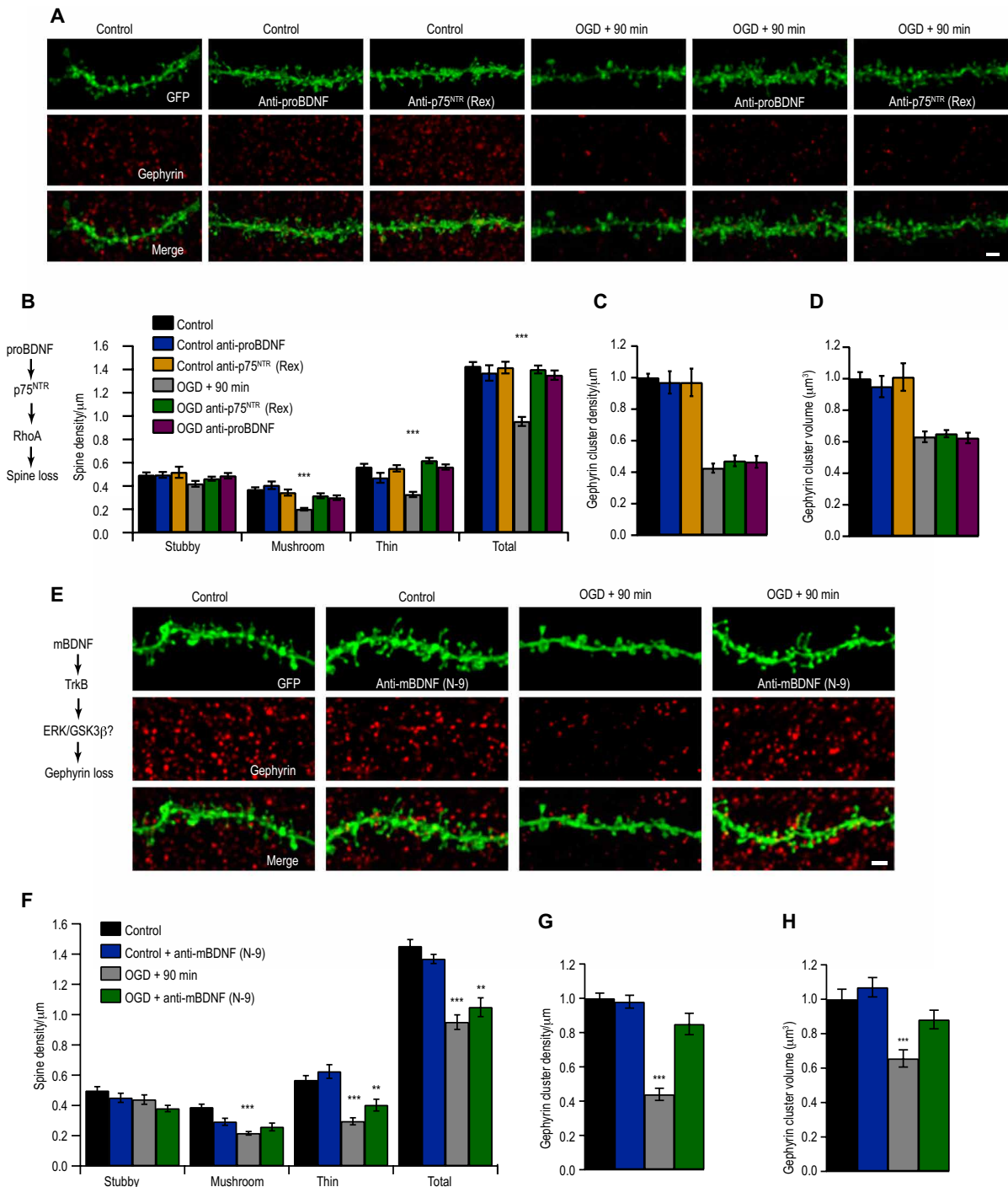
Fig. 3. Differential proBDNF and mBDNF signaling induce synapse loss after ischemia. (**A**) Example CA1 tertiary dendrites immunostained for gephyrin, with or without anti-proBDNF or anti-p75^{NTR} (Rex) treatment before OGD. Scale bar, 2 μm. (**B**) Dendritic spine quantification (***$P < 0.001$). Total spine density (spines per micrometer): Control, 1.43 ± 0.04; Control + anti-proBDNF, 1.37 ± 0.07; Control + anti-p75 ^{NTR}, 1.42 ± 0.05; OGD, 0.95 ± 0.04; OGD + anti-proBDNF, 1.40 ± 0.03; OGD + anti-p75^{NTR}, 1.35 ± 0.04. (**C**) Quantification of gephyrin cluster density ($P = 0.28$). Mean number (A.U.): Control, 1.00 ± 0.03; Control + anti-proBDNF, 0.97 ± 0.07; Control + anti-p75^{NTR}, 0.97 ± 0.06; OGD, 0.43 ± 0.03; OGD + anti-proBDNF, 0.47 ± 0.03; OGD + anti-p75^{NTR}, 0.47 ± 0.04 ($n = 9$). (**D**) Quantification of gephyrin puncta volume ($P = 0.57$). Mean volume (A.U.): Control, 1.00 ± 0.04; Control + anti-proBDNF, 0.95 ± 0.07; Control + anti-p75^{NTR}, 1.01 ± 0.09; OGD, 0.63 ± 0.03; OGD + anti-proBDNF, 0.65 ± 0.02; OGD + anti-p75^{NTR}, 0.62 ± 0.03. (**E**) CA1 tertiary dendrites immunostained for gephyrin, with or without anti-mBDNF (N-9) treatment before OGD. (**F**) Quantification of spines (**$P < 0.01$, ***$P < 0.001$). Total spine density (spines per micrometer): Control, 1.45 ± 0.04; Control + anti-mBDNF (N-9), 1.37 ± 0.03; OGD, 0.95 ± 0.05; OGD + anti-N-9, 1.05 ± 0.06. (**G**) Quantification of number of gephyrin clusters (***$P < 0.001$). Mean number (A.U.): Control, 1.00 ± 0.03; Control + N-9, 0.99 ± 0.04; OGD, 0.44 ± 0.04; OGD + anti-mBDNF (N-9), 0.85 ± 0.06. (**H**) Quantification of gephyrin cluster volume (***$P < 0.001$). Mean volume (A.U.): Control, 1.00 ± 0.06; Control + N-9, 1.07 ± 0.06; OGD, 0.66 ± 0.05; OGD + N-9, 0.88 ± 0.05. Data are shown as means ± SD. Two-way ANOVA with Bonferroni multiple comparison test. $n = 18$ slices.

suggested that mBDNF was not mediating excitatory synapse loss after OGD. In contrast, anti-mBDNF treatment was sufficient to prevent the reduction of gephyrin cluster density in OGD-treated slices (Fig. 3G). Reduction of gephyrin cluster volume was also prevented in the presence of anti-mBDNF antibody compared to OGD slices (Fig. 3H). Our results show that mBDNF acts specifically on GABAergic synapses after OGD.

We confirmed the specificity of proBDNF in modulating excitatory synapses and mBDNF signaling modulating gephyrin. Application to organotypic hippocampal cultures with proBDNF (100 ng/ml for 90 min) specifically reduces glutamatergic spine synapses and mBDNF (100 ng/ml for 90 min) reduced only GABAergic synapses (fig. S2, E to H′). These data reveal the specificity of proBDNF in excitatory synapse regulation and mBDNF in inhibitory synapse modulation.

Blocking ERK1/2 and GSK3β pathways protects gephyrin, but not dendritic spine loss

mBDNF binds with high affinity to TrkB receptors. It is also known that ERK1/2 and GSK3β pathways are activated downstream of TrkB. Therefore, we determined whether ERK1/2 and GSK3β signaling cascades downstream of TrkB were activated after OGD to mediate gephyrin cluster reduction at GABAergic terminals. We pretreated slices with pharmacological inhibitors of GSK3β (25 μM GSK3β-IX) and mitogen-activated protein kinase kinase (MEK) (30 μM PD98059) to prevent activation of these kinases before OGD. Control treated and untreated cultures served for comparative analysis. As expected, inhibiting ERK1/2 and GSK3β pathways did not prevent dendritic spine loss in OGD-treated cultures (Fig. 4, A and B). Specifically, the mushroom and stubby dendritic spines that were most affected by OGD could not be rescued with ERK1/2 and GSK3β blockade (Fig. 4B). However, at GABAergic synapses, gephyrin cluster loss was prevented after OGD in slices pretreated with GSK3β-IX and PD98059, compared to untreated OGD slices (Fig. 4, A, C, and D).

We assessed the individual effects of GSK3β-IX or PD98059 treatment during MCAO on gephyrin clustering. In control hippocampal slices, GSK3β-IX treatment increased cluster density, but in MCAO slices, we had to block both GSK3β and ERK1/2 pathways to effectively prevent the loss of gephyrin cluster density (fig. S3B). When we quantified changes in gephyrin cluster volume, we found that in control slices treated with PD98059, the volume of gephyrin puncta significantly increased. However, in MCAO treated slices, blocking either GSK3β or ERK1/2 pathways prevented the loss of gephyrin puncta volume (fig. S3C).

Previously, we have reported that GSK3β phosphorylates gephyrin on Ser[270] to negatively regulate the number of gephyrin clusters (25) and ERK1/2 phosphorylates gephyrin at Ser[268] to negatively regulate the size of gephyrin clusters (26). To determine whether phosphorylation of these serine residues was important for OGD-induced gephyrin down-regulation, we used biolistic transfection of GFP-tagged gephyrin where Ser[268] and Ser[270] were mutated to alanines (gephyrin$_{S268A/S270A}$) into CA1 pyramidal neurons and assessed whether this gephyrin mutant is insensitive to mBDNF-mediated TrkB signaling after OGD. Our analysis showed that gephyrin$_{S268A/S270A}$ mutant is resistant to OGD compared to WT gephyrin (gephyrin$_{WT}$) (Fig. 4, E, F, H, and I). Transgene expression of gephyrin$_{S268A/S270A}$ mutant could not prevent dendritic spine loss after OGD, which is consistent with the data using pharmacological inhibitors that block kinase pathways directly phosphorylating gephyrin at Ser[268] and

Ser[270], respectively (Fig. 4G). Overall, our results identify gephyrin phosphorylation at Ser[268] and Ser[270] downstream of TrkB as a determinant for GABAergic synapse loss after OGD.

The MCAO model in vivo recapitulates OGD-induced synapse loss at 24 hours after ischemia

To confirm our results in in vivo, we used MCAO technique, in which an intraluminal filament is used to cause transient ischemia in the frontal-parietal cortex and striatum (27) and assayed for glutamatergic and GABAergic synapse loss 24 hours after MCAO. MCAO is the most extensively used model in rodents as it produces a reproducible infarct (core and peri-infarct area) where pathophysiological cascades are well described. The peri-infarct area surrounding the core is the site for inflammation, synaptic plasticity, and circuit adaptations where structural and functional changes within cortex have been observed in patients after 3 months following an anterior ischemic stroke (28). Cell death within the ischemic core renders the tissue fragile for morphology or functional analysis; hence, we restricted our analysis to the penumbra.

We used immunohistochemical staining to assess changes in glutamatergic and GABAergic synapse changes within the peri-infarct area and in the corresponding area contralaterally as comparison. For glutamatergic synapse labeling, we chose vesicular glutamate transporter 1 (VGLUT1) to test for glutamatergic presynaptic changes and PSD95 for glutamatergic postsynaptic changes (Fig. 5, A to C). For GABAergic synapse labeling, we chose GAD65/67 (glutamic acid decarboxylase/65-kilodalton isoform/67-kilodalton isoform) to label presynaptic terminals: GABA$_A$R γ2 for synaptic receptors and GABA$_A$R α5 for extrasynaptic receptors (Fig. 5, A, D, E, and F). Analysis of parietal cortex layer 2/3 (L2/3) 24 hours after MCAO did not show any observable loss of PSD95 (Fig. 5C). This result is consistent with previous report that, under ischemic conditions, neuronal nitric oxide synthase (nNOS) interacts with PSD95 to stabilize it at the cell membrane (29). Analysis for VGLUT1-positive terminals showed a significant reduction in presynaptic sites in both ipsi- and contralateral hemispheres (Fig. 5B).

At GABAergic synapses, we saw a significant reduction in GAD65/67 terminals, γ2 subunit–containing synaptic GABA$_A$Rs, and α5 subunit–containing extrasynaptic GABA$_A$Rs (Fig. 5, D to F). We could not morphologically assess for α1 and α2 subunit–containing GABA$_A$Rs in MCAO tissue due to the strong postfixation protocol that is not conducive for these two antibodies. Therefore, we used Western blot (WB) to examine the expression level of α1 and α2 subunits in control and MCAO tissue from both ipsi- and contralateral hemispheres of parietal cortex L2/3. We found a significant reduction in α1 and α2 GABA$_A$R subunit expression after MCAO (fig. S4, A and B). Overall, our analysis confirms that both ipsi- and contralateral hemispheres decrease protein expression of important glutamatergic and GABAergic synaptic markers. Therefore, reduced excitatory and inhibitory synapse markers in vivo recapitulate our in vitro OGD results, showing impaired glutamatergic and GABAergic synaptic transmission.

Blocking effector kinases downstream of TrkB in vitro OGD experiments effectively rescued GABAergic synapse loss (Fig. 4, C and D) and transgene expression of gephyrin S268A/S270A mutant insensitive to ERK1/2 and GSK3β kinases prevented gephyrin cluster loss after OGD (Fig. 4, H and I). Hence, we assessed ERK1/2 and GSK3β kinase activation levels 24 hours after MCAO in frontal-parietal cortex ipsi- and contralaterally in BL6 WT mice. WB analysis for
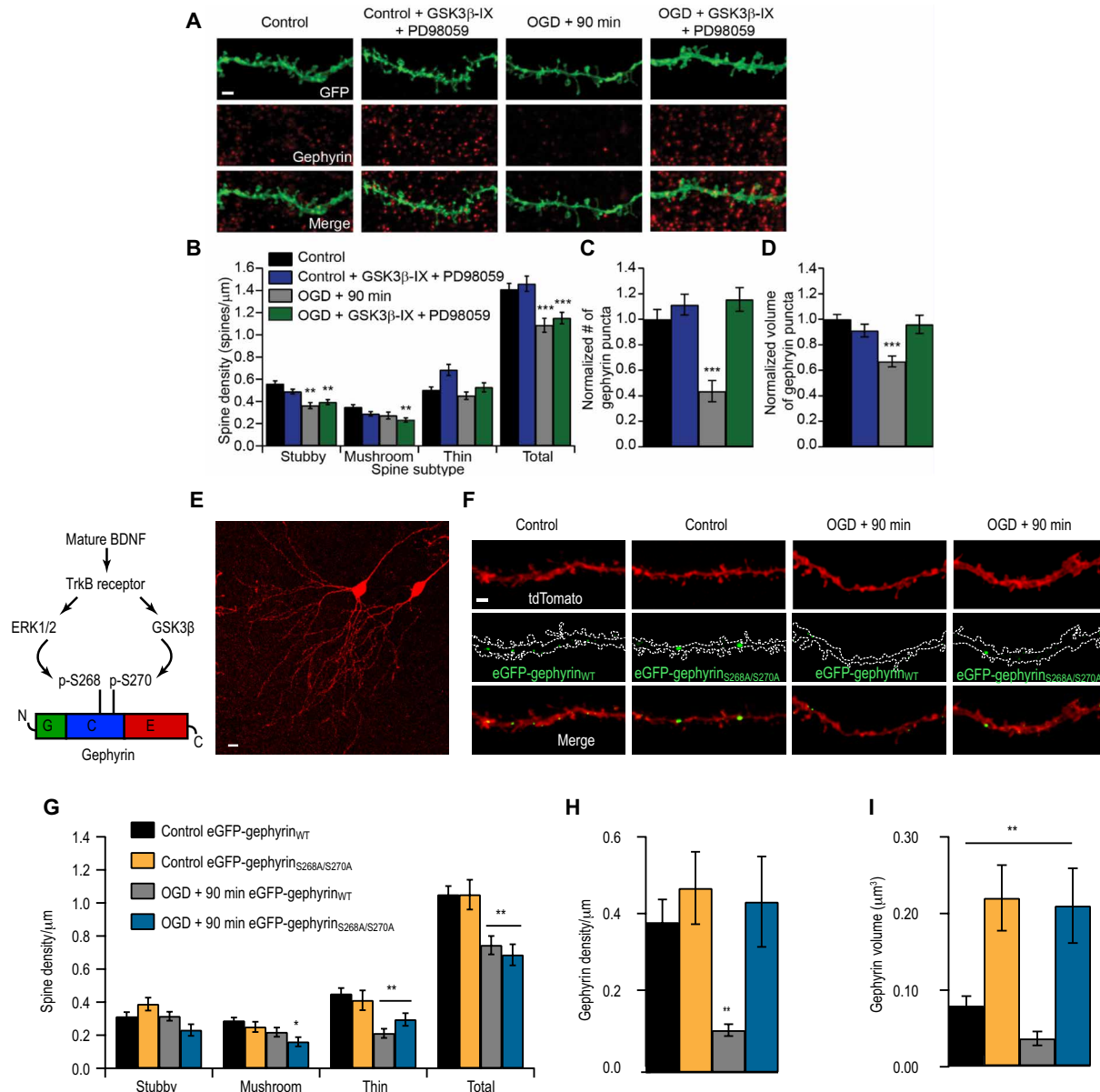
Fig. 4. ERK1/2 and GSK3β pathways induce gephyrin degradation but not dendritic spine loss after OGD. (**A**) Example CA1 tertiary dendrites from control and 90 min after OGD slices, immunostained for gephyrin, with or without GSK3β-IX and PD98059. Scale bar, 2 μm. (**B**) Spine quantification (**$P < 0.01$, ***$P < 0.001$). Total spine density (spines per micrometer): Control, 1.41 ± 0.06; Control + PD + G.-IX, 1.46 ± 0.07; OGD, 1.09 ± 0.06; OGD + PD + G.-IX, 1.15 ± 0.05. (**C**) Quantification of gephyrin cluster density (***$P < 0.001$). (**D**) Quantification of gephyrin cluster volume. Mean number (A.U.): Control, 1.00 ± 0.08; Control + PD + G.-IX, 1.12 ± 0.08; OGD, 0.44 ± 0.08; OGD + PD + G.-IX, 1.16 ± 0.09 (***$P < 0.001$). Mean volume (A.U.): Control, 1.00 ± 0.04; Control + PD + G.-IX, 0.91 ± 0.05; OGD, 0.67 ± 0.04; OGD + PD + G.-IX, 0.96 ± 0.07. (**E**) Example CA1 pyramidal neurons biolistically transfected with tdTomato and gephyrin. Scale bar, 10 μm. (**F**) CA1 tertiary dendrites from control and 90 min after OGD slices transfected with either eGFP-gephyrin$_{WT}$ or eGFP-gephyrin$_{S268A/S270A}$. (**G**) Spine quantification (*$P < 0.05$, **$P < 0.01$). Total spine density (spines per micrometer): Control + gephyrin$_{WT}$-GFP, 1.05 ± 0.052; Control + eGFP-gephyrin$_{S268A/S270A}$, 1.05 ± 0.090; OGD, eGFP-gephyrin$_{WT}$ 0.74 ± 0.056; OGD + eGFP-gephyrin$_{S268A/S270A}$, 0.69 ± 0.064. (**H**) Gephyrin cluster density (**$P < 0.01$). Density: Control + eGFP-gephyrin$_{WT}$, 0.38 ± 0.58; Control + eGFP-gephyrin$_{S268A/S270A}$, 0.47 ± 0.092; OGD + eGFP-gephyrin$_{WT}$, 0.11 ± 0.015; OGD+ eGFP-gephyrin$_{S268A/S270A}$, 0.44 ± 0.12. (**I**) Gephyrin cluster volume (**$P < 0.01$). Mean volume: Control + eGFP-gephyrin$_{WT}$, 0.85 ± 0.012; Control + eGFP-gephyrin$_{S268A/S270A}$, 0.22 ± 0.043; OGD + eGFP-gephyrin$_{WT}$, 0.046 ± 0.01; OGD+ eGFP-gephyrin$_{S268A/S270A}$, 0.21 ± 0.049. Data are shown as means $\pm$ SD. Two-way ANOVA with Bonferroni multiple comparison test. $n = 18$ slices.

ERK1/2 and its phosphorylated form showed unchanged ERK1/2 levels but significantly increased levels of phosphorylated ERK1/2 in the ipsilateral but not the contralateral hemisphere at 24 hours after MCAO (Fig. 5, G and H). WB analysis for GSK3β showed increased kinase expression in the contralateral hemisphere but not the ipsilateral hemisphere at 24 hours after MCAO (Fig. 5I). Gephyrin expression level and its phosphorylation at Ser^{268} and Ser^{270} sites changed at 24 hours after MCAO (Fig. 5, J to J‴). WB quantification confirmed that total gephyrin protein levels significantly decrease at 24 hours after MCAO (Fig. 5J′). Consistent with our observation of elevated
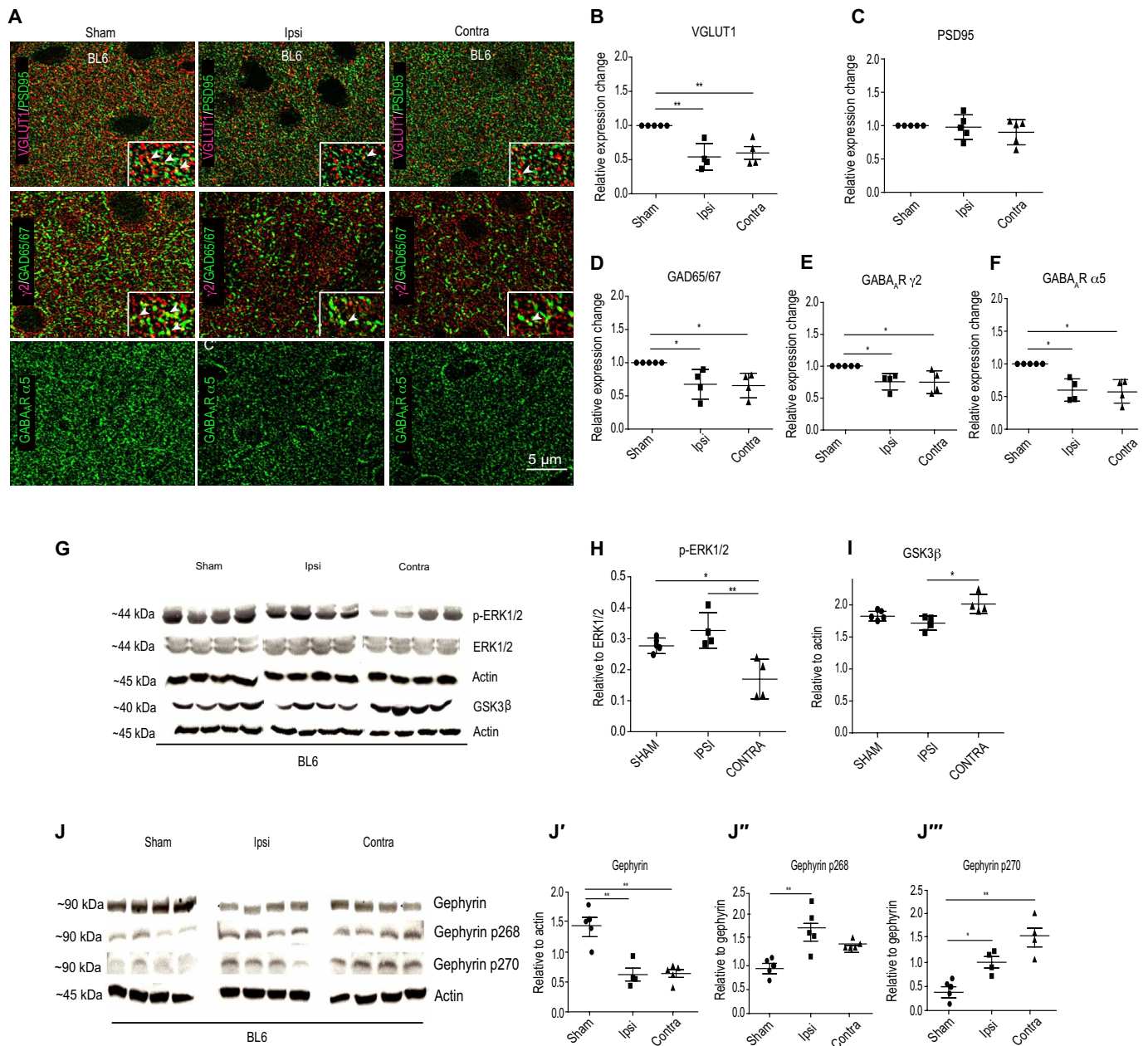
Fig. 5. Synapse changes in the peri-infarct area of ipsilateral hemispheres 24 hours following MCAO. (**A**) Example composite images for glutamatergic synaptic proteins (VGLUT1 and PSD95) and GABAergic synaptic markers (GAD65/67, GABA_AR γ2, and GABA_AR α5). (**B**) Quantification for VGLUT1 cluster density [one-way ANOVA, Bonferroni multiple comparison post hoc test; $F_{2,49} = 11.2$; $**P < 0.01$]. (**C**) Quantification for PSD95 cluster density [one-way ANOVA, Bonferroni multiple comparison post hoc test; $F_{2,49} = 0.84$; $P = 0.43$]. (**D** to **F**) Quantification for GAD65/67 [one-way ANOVA, Bonferroni multiple comparison post hoc test; $F_{2,10} = 7.9$; $P = 0.0085$], GABA_AR γ2 [one-way ANOVA, Bonferroni multiple comparison post hoc test; $F_{2,9} = 6.4$; $P = 0.018$], and GABA_AR α5 cluster density (one-way ANOVA, Bonferroni multiple comparison test; $F_{2,9} = 8.3$; $P = 0.0088$). Data are shown as means ± SD ($n = 5$ animals); $*P < 0.05$. (**G** to **I**) WB analysis for phospho-ERK1/2, total ERK1/2, GSK3β, and actin in sham and 24 hours after MCAO samples. $*P < 0.05$, $**P < 0.01$. (**J** to **J‴**) WB analysis for total gephyrin, phospho-gephyrin at Ser[268] (gephyrin p268), and phospho-gephyrin at Ser[270] (gephyrin p270) levels in BL6 WT sham and 24 hours after MCAO mice. $*P < 0.05$, $**P < 0.01$. Data are shown as means ± SD ($n = 4$ animals).

ERK1/2 activation on the ipsilateral hemisphere, we observed significantly higher Ser[268] phosphorylation on gephyrin (Fig. 5J″). Similarly, higher GSK3β levels in the contralateral hemisphere correlated with significantly higher Ser[270] phosphorylation on gephyrin (Fig. 5J‴). These observations are consistent with our in vitro OGD data and further confirm a role for ERK1/2 and GSK3β pathways in directly phosphorylating gephyrin to regulate protein stability after MCAO.

Synapse loss after MCAO is attenuated in *Gphn*S268A/S270A point mutant mice

To obtain a more direct confirmation for the central role of gephyrin phosphorylation in synapse alterations 24 hours after MCAO, we generated a *Gphn*S268A/S270A global point mutant mouse line using CRISPR-Cas9 (Cyagen). First, we assessed for baseline changes in glutamatergic and GABAergic synaptic markers. For this, we

stained for VGLUT1 and PSD95 or GABA$_A$R γ2 subunit and GAD65/67 (Fig. 6A). Quantification confirmed that synapse distribution and density for glutamatergic and GABAergic synapses in our *Gphn*S268A/S270A global point mutant mouse are not altered in comparison to WT littermate controls (Fig. 6, B to D′). Having established this, we performed MCAO in *Gphn*S268A/S270A mutant mice and compared synapse plasticity changes in the parietal cortex L2/3 with sham *Gphn*S268A/S270A littermates. We analyzed for changes in glutamatergic and GABAergic synaptic markers using immuno-histochemical analysis 24 hours after MCAO (Fig. 6). In the *Gphn*S268A/S270A mutant mice, we observed stabilization of excitatory VGLUT1-positive terminals on both ipsi- and contra-lateral hemispheres 24 hours after MCAO (Fig. 6, E to F′). PSD95 cluster density was also unchanged in the ipsi- and the contralateral hemispheres (Fig. 6F′). Analysis of GABAergic synaptic markers showed a significant increase in the GAD65/67 puncta density in both ipsi- and contralateral hemispheres (Fig. 6G). Significantly, we did not observe any reduction in γ2- and α5-containing GABA$_A$Rs in *Gphn*268/S270A mutant mice 24 hours after MCAO (Fig. 6, G′ and G″). Consistent with observed synaptic marker changes, WB analysis for the α1 and α2 subunits in *Gphn*268/S270A mutant mice showed no alterations for these two major GABA$_A$R subunits 24 hours following MCAO (fig. S4, C and D). Together, these results substantiate an involvement of ERK1/2 and GSK3β as downstream effectors that critically influence gephyrin scaffold stability along with glutamatergic and GABAergic synapse integrity after MCAO.

Microglia facilitate synapse loss after MCAO

While it is well established that BDNF levels increase after cerebral ischemia, the source of BDNF after stroke remains unclear. Given that *Bdnf* transcripts have been localized within microglia (*30*), we wondered whether microglia contributed to BDNF signaling after stroke. We assessed for BDNF protein changes within IBA1-positive cells corresponding to microglia using near super-resolution Airyscan microscopy analysis of sham and MCAO BL6 WT mice. Under baseline sham condition, we found low BDNF colocalization within IBA1 microglia (Fig. 7, A and A′). However, following MCAO, we could detect elevated BDNF protein within both soma and processes on both ipsi- and contralateral hemispheres (Fig. 7A). Quantification confirmed an increase in BDNF protein within microglia at 24 hours after MCAO (Fig. 7A′), implicating elevated BDNF protein translation within microglia in the synaptic pathology of stroke.

To directly examine the role of microglia in BDNF synthesis and synaptic changes after MCAO, we next sought to deplete microglia from the brain using the pharmacological inhibitor PLX5622 that targets colony-stimulating factor 1 receptor phosphorylation in microglia (Plexxikon Inc.). It has been reported that prolonged administration of this drug (1 week) in a formulated chow diet depletes 90% of the microglia from rodent brain (*31*, *32*). Replacing the mice on regular diet repopulates microglia cells within 5 to 7 days. No adverse changes to synapse structure and function or transcriptional changes have been reported after PLX5622 chow administration (*33*). We confirmed the loss of microglia after PLX5622 chow administration after 7 days (Fig. 6, B and B′).

To test whether microglia contribute to synaptic changes observed at 24 hours after MCAO, we treated BL6 WT with PLX5622 formulated chow or control chow. We then assessed for synapse alterations

by staining for synaptic markers and found no significant differences in either glutamatergic synaptic markers (VGLUT1 and PSD95) or GABAergic synaptic markers (GAD65/67, GABA$_A$R α5, and GABA$_A$R γ2) between the groups (Fig. 7, C to H). Similarly, WB analysis to assess α1 or α2 GABA$_A$R subunit expression showed no changes at 24 hours after MCAO in mice administered with PLX5622 (fig. S4, E and F). In addition, WB analysis to assess total gephyrin or changes in gephyrin phosphorylation at Ser^{268} and Ser^{270} in PLX5622-treated mice showed no changes (Fig. 7, I to I‴). These findings point to the critical role of microglia in mediating synapse loss after MCAO.

Microglia release BDNF after MCAO to facilitate synapse loss

BDNF has been shown to play a critical role in the activation of microglia in vitro, and increase in BDNF has been tightly linked to proinflammation responses (*34*, *35*). To specifically evaluate the role of BDNF within microglia in synapse loss following MCAO, we used CX3CR1$^{ERT2Cre+/−}$ mice specifically expressing tamoxifen-inducible Cre recombinase in microglia cells and generated BDNF$^{flox/flox}$/CX3CR1$^{CreERT2+/−}$ conditional knockout (cKO) mouse line, thereby preventing *Bdnf* expression selectively in microglia. We used BDNF$^{wt/wt}$ and BDNF$^{flox/flox}$ mice to culture microglia from postnatal day 3 pups to confirm *Bdnf* gene deletion in microglia cells. Quantitative reverse transcription polymerase chain reaction analysis confirmed significant reduction in microglial *Bdnf* mRNA specifically from BDNF$^{flox/flox}$ mice (fig. S5A). The observed 30% mRNA reduction in vitro is merely due to the (commonly accepted) scarce efficiency of viral transduction in microglia. Next, we confirmed the loss of BDNF protein from BDNF$^{flox/flox}$/CX3CR1$^{CreERT2+/−}$ mice in vivo as tamoxifen-induced CRE nuclear translocation (in Cx3cr1^{CREert2} mice), resulting in more than 90% efficiency. We stained for BDNF and IBA1 in brain slices from BDNF$^{wt/wt}$/CX3CR1$^{CreERT2+/−}$ and BDNF$^{flox/flox}$/CX3CR1$^{CreERT2+/−}$ mice. We observed BDNF colocalization in microglia soma and processes in the BDNF$^{wt/wt}$/CX3CR1$^{CreERT2+/−}$ tissue but not in BDNF$^{flox/flox}$/CX3CR1$^{CreERT2+/−}$ mice tissue (fig. S5, B and B′).

Having confirmed that our cKO mouse line efficiently deletes BDNF in microglia cells, we examined the contribution of microglia *Bdnf* to synaptic changes observed at 24 hours after MCAO. For this, we assessed changes in synaptic markers (VGLUT1, GAD65/67, GABA$_A$R γ2, and GABA$_A$R α5) in both ipsi- and contralateral hemispheres at 24 hours after MCAO compared to BDNF$^{flox/flox}$/CX3CR1$^{CreERT2+/−}$ sham animals. There were no significant changes between the MCAO and sham groups (fig. S5, C to H). We also performed WB analysis to measure α1 and α2 GABA$_A$R subunit expression level changes between MCAO and sham group (fig. S4, G and H). Our analysis confirmed that the synaptic receptor expression is unchanged upon *Bdnf* gene depletion from microglia cells after MCAO. Our earlier observation showed stabilized gephyrin protein levels and no increase in gephyrin phosphorylation at Ser^{268} and Ser^{270} after microglia depletion using PLX5622 (Fig. 7, I to I‴). To confirm whether microglial BDNF signaling led to gephyrin protein loss and elevated phosphorylation at Ser^{268} and Ser^{270} residues, we performed WB analysis using tissue from BDNF$^{flox/flox}$/CX3CR1$^{CreERT2+/−}$ sham and MCAO animals (fig. S5, I to I‴). The WB analysis showed that total gephyrin levels and gephyrin phosphorylation at Ser^{270} were unchanged, while gephyrin phosphorylation at Ser^{268} is reduced after MCAO. Our results uncover a consistent pattern of gephyrin stabilization, reduced gephyrin phosphorylation at Ser^{268} and Ser^{270}
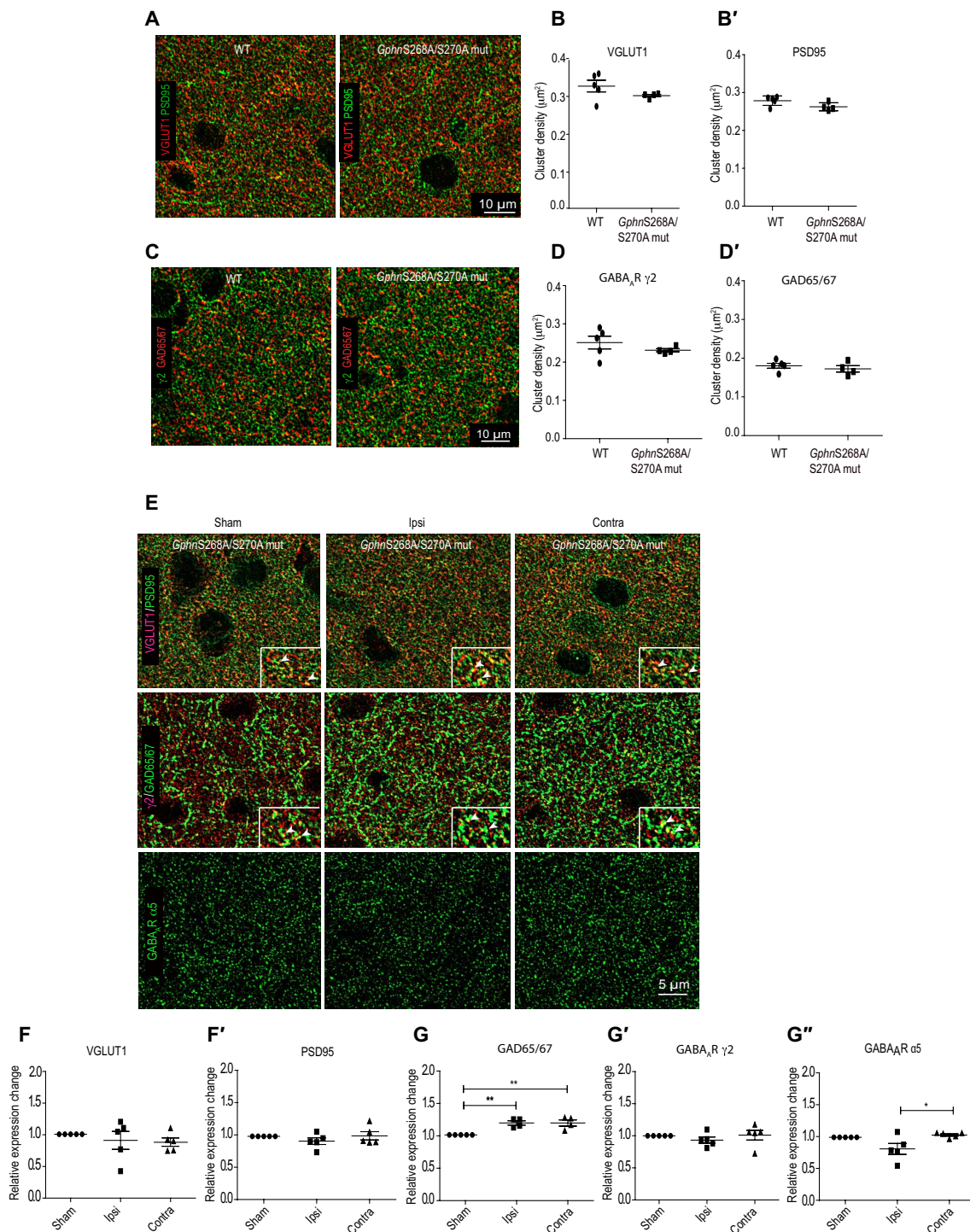
Fig. 6. Synapse loss is attenuated in *Gphn*S268A/S270A mutant mice 24 hours following MCAO. (**A**) Example images of immunohistochemical staining for glutamatergic synapse marker proteins from motor cortex L2/3 ipsi- and contralateral sides in WT and *Gphn*S268A/S270A mutant mice. (**B** and **B′**) Quantification of VGLUT1 and PSD95 cluster density per square micrometer. (**C**) Example images of immunohistochemical staining for GABAergic synapse marker proteins from motor cortex L2/3 ipsi- and contralateral sides in WT and *Gphn*S268A/S270A mutant mice. (**D** and **D′**) Quantification of GABA$_A$R γ2 subunit and GAD65/67 cluster density per square micrometer. (**E**) Example images of immunohistochemical staining for glutamatergic and GABAergic synaptic proteins in *Gphn*S268A/S270A mutant mice 24 hours following MCAO. Glutamatergic synaptic terminals were visualized using VGLUT1 and PSD95 (see insets). GABAergic synaptic sites were visualized using GAD65/67, GABA$_A$R γ2, and GABA$_A$R α5. (**F**) Quantification for VGLUT1 [one-way ANOVA, Brown-Forsythe test; $F_{2,11} = 0.35$; $P = 0.70$]. (**F′**) Quantification of PSD95 cluster density [one-way ANOVA, Brown-Forsythe test; $F_{2,11} = 1.03$; $P = 0.38$]. (**G**) Quantification for GAD65/67 [one-way ANOVA, Bonferroni multiple comparison test; $F_{2,9} = 11.9$; $P = 0.003$]. **$P < 0.01$. (**G′**) Quantification of GABA$_A$R γ2 [one-way ANOVA, Bonferroni multiple comparison test; $F_{2,11} = 0.60$; $P = 0.56$]. (**G″**) Quantification of GABA$_A$R α5 clusters [one-way ANOVA, Bonferroni multiple comparison test; $F_{2,11} = 4.9$; $P = 0.02$]. *$P < 0.05$. Data are shown as means ± SD ($n = 5$ animals).
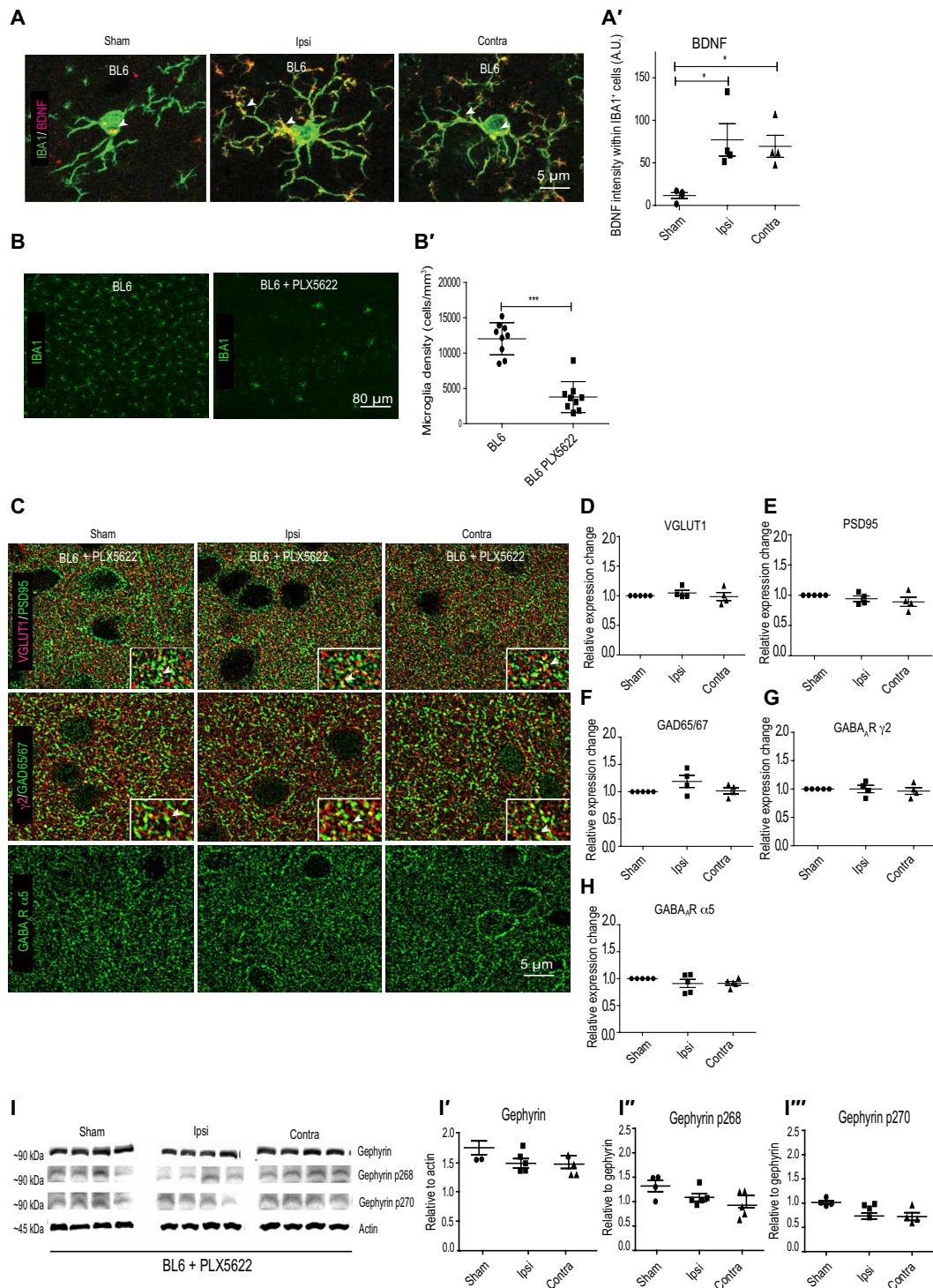
Fig. 7. Microglia depletion stabilizes synapse changes after OGD. (**A**) BDNF expression within microglia in BL6 WT sham and MCAO animals. (**A′**) Quantification of BDNF intensity within IBA1-positive cells. *$P < 0.05$. (**B**) Example images from BL6 WT mice treated with PLX5622 sham and MCAO. (**B′**) Microglia depletion after PLX5622 chow treatment for 7 days (chow, 1200 mg/kg). ***$P < 0.001$. (**C**) Example images from BL6 WT PLX5622-treated MCAO animals, quantified for (**D** and **E**) VGLUT1 and PSD95 and (**F** to **H**) GAD65/67, GABA$_A$R γ2, and GABA$_A$R α5 expression changes relative to sham in BL6 WT PLX5622-treated MCAO animals. (**I**) WB analysis for total gephyrin, phospho-gephyrin at Ser[268], and phospho-gephyrin at Ser[270] levels in BL6 WT mice treated with PLX5622 at 24 hours after MCAO. (**I′** to **I‴**) Quantification of WB for total gephyrin, phospho-gephyrin at Ser[268] and phospho-gephyrin at Ser[270] levels in BL6 WT mice treated with PLX5622 at 24 hours after MCAO. Quantification expressed as means ± SD ($n = 5$); $P > 0.05$ (one-way ANOVA, Bonferroni multiple comparison test).

residues and synapse preservation at 24 hours after MCAO in BL6 mice treated with PLX5622 and BDNF$^{flox/flox}$/CX3CR1$^{CreERT2+/−}$ transgene mice, suggesting that microglia-derived BDNF signals for gephyrin phosphorylation and subsequent synapse down-regulation at 24 hours after MCAO.

GphnS268A/S270A mutation or Bdnf deletion from microglia reduces brain damage after MCAO

While BDNF has been shown to play the role of prosurvival factor, including microglia activation in vivo (36), there is evidence to suggest that neuronal activity–dependent exocytosis and/or release from microglia can contribute to specific conditions of brain pathology. To test this, we performed MCAO in BL6 WT mice, BL6 WT mice treated with PLX5622, GphnS268A/S270A mutant mice, or BDNF$^{flox/flox}$/CX3CR1$^{CreERT2+/−}$ cKO mice (Fig. 8, A and B). We used cresyl violet staining to measure the infarct volume across brain sections 24 hours following MCAO. Quantification confirmed that, in GphnS268A/S270A mutant mice and BDNF$^{flox/flox}$/CX3CR1$^{CreERT2+/−}$ cKO mice, the ischemic tissue damage was significantly reduced as compared to BL6 WT mice. We see a trend in reduced infarct volume in PLX5622-treated mice that does not reach significance. It is likely that ablating microglia completely causes compensatory adaptations in the brain that are not identical to microglia-specific Bdnf gene deletion. These results support our idea that prevention of microglia BDNF release after ischemia or blocking its downstream phosphorylation target gephyrin enhances tissue preservation 24 hours after MCAO.

In vivo inflammatory processes play a key role in tissue damage and repair. In response to inflammation, microglia acquire properties for reactive species generation and inflammatory cytokine production and are therefore thought to be principal drivers of proinflammatory responses (37, 38). Given that GphnS268A/S270A mutant mice show enhanced tissue preservation 24 hours after MCAO, we anticipated gephyrin scaffold stabilization to reduce microglia activation after MCAO. To assess microglia properties, we first examined the density of resident microglia at baseline and 24 hours after MCAO in the brains of BL6 WT and GphnS268A/S270A mutant mice (Fig. 8, C and D). Quantification of IBA1-positive microglia showed a significant reduction of microglia density from both ipsi- and contralateral hemispheres after MCAO in BL6 WT mice (Fig. 8C′). Similarly, analyzing for area covered by the microglia cells showed significant reduction in both ipsi- and contralateral sides (Fig. 8C″). These observed changes are consistent with the report showing changes in microglia migration after stroke (38). To confirm inflammation induced microglia activation at 24 hours after MCAO, we stained for the activation-state marker CD11b in microglial cells. Quantification for CD11b intensity showed elevated levels only on the ipsilateral but not the contralateral side in BL6 WT mice (Fig. 8C‴). Analysis of microglia density in GphnS268A/S270A mutant mice showed no changes between sham and MCAO samples (Fig. 8D′). Similarly, there was no change in the area covered (Fig. 8D″). If gephyrin scaffold stabilization leads to reduced microglia activation, then we anticipated less activation of microglia in GphnS268A/S270A mutant mice after MCAO. Analysis for CD11b intensity was not elevated after MCAO in the GphnS268A/S270A mutant mice (Fig. 8D‴). Together, our data show that in Gphn268/S270A mutant mice, the mutation selectively blocks MCAO-induced microglia activation and reduces ischemic tissue damage.

BDNF deletion from microglia or GphnS268A/S270A mutation prevents BDNF increase

If gephyrin scaffold stability contributes toward microglia activation after MCAO, then it should be reflected in proBDNF and mBDNF level changes in our different mouse lines. As a first step, we assessed for differences in the baseline level of proBDNF and mBDNF across our different mouse lines. WB analysis showed that BL6 WT mice treated with PLX5622 had elevated levels of proBDNF and BDNF$^{flox/flox}$/CX3CR1$^{CreERT2+/−}$ mice exhibited significantly lower levels of proBDNF, while others had levels similar to BL6 WT control (fig. S6, A and A′). The analysis of mBDNF across different mice lines showed no significant differences (fig. S6, A and A″).

Once we established the baseline differences in proBDNF and mBDNF expression across mice lines used in our study, we went on to compare intramouse changes in proBDNF and mBDNF within ipsi- and contralateral hemispheres 24 hours after MCAO. In BL6 WT mice, we observed a significant increase in both pro and mature forms of BDNF specifically in the ipsilateral side; there was a small increase in the contralateral side, but it was not statistically significant (fig. S6, B to B″). In BL6 WT mice treated with PLX5622, we saw a significant reduction of proBDNF levels in both hemispheres 24 hours after MCAO compared to sham group (fig. S6, C and C′). This reduction suggests that resident microglia themselves are an important source of proBDNF or alternatively that microglia signal for proBDNF release elsewhere following MCAO. Levels of mBDNF showed no changes within both ipsi- and contralateral hemispheres in PLX5622-treated mice (fig. S6C″). In BDNF$^{flox/flox}$/CX3CR1$^{CreERT2+/−}$ cKO, although proBDNF levels were significantly lower than BL6 WT animals at baseline, there was no significant difference within the genotype after MCAO (fig. S6, D and D′). However, mBDNF that was at similar levels to BL6 WT showed a significant reduction in both ipsi- and contralateral hemispheres after MCAO within the genotype (fig. S6, D to D″). We then assessed BDNF level changes in the GphnS268A/S270A mutant mice. Quantification of the WB showed that gephyrin scaffold stabilization prevented the ipsilateral increase in proBDNF and mBDNF levels observed in BL6 WT animals after MCAO (fig. S6, E to E″). These observations suggests that (i) microglia are an important source of BDNF after MCAO and that (ii) microglial proBDNF and mBDNF release is influenced by the phosphorylation status of gephyrin at Ser^{268} and Ser^{270} following MCAO.

To obtain further evidence that BDNF protein increase occurs within microglia cells at 24 hours after MCAO, we used near super-resolution Airyscan microscopy and stained for microglia using IBA1 and BDNF. First, we tested for BDNF changes under sham and MCAO conditions using BDNF$^{WT/WT}$/CX3CR1$^{CreERT2+/−}$ mice. A weak BDNF staining within IBA1-positive cells was observed under sham conditions; however, significantly stronger BDNF staining was seen within the ipsi- and contralateral hemispheres at 24 hours after MCAO (Fig. 9, A and A′). When we deleted Bdnf gene within microglia cells using BDNF$^{flox/flox}$/CX3CR1$^{CreERT2+/−}$ mice, we could not detect BDNF protein under sham or MCAO conditions (Fig. 9, B and B′). This further confirms that microglia can produce BDNF on demand. We also tested for BDNF changes within microglia in our GphnS268A/S270A mutant mice. Consistent with our finding that gephyrin mutation affects microglia activation (Fig. 8, D to D‴), we uncovered that GphnS268A/S270A mutation blocks BDNF increase within microglia cells after MCAO (Fig. 9, C and C′).
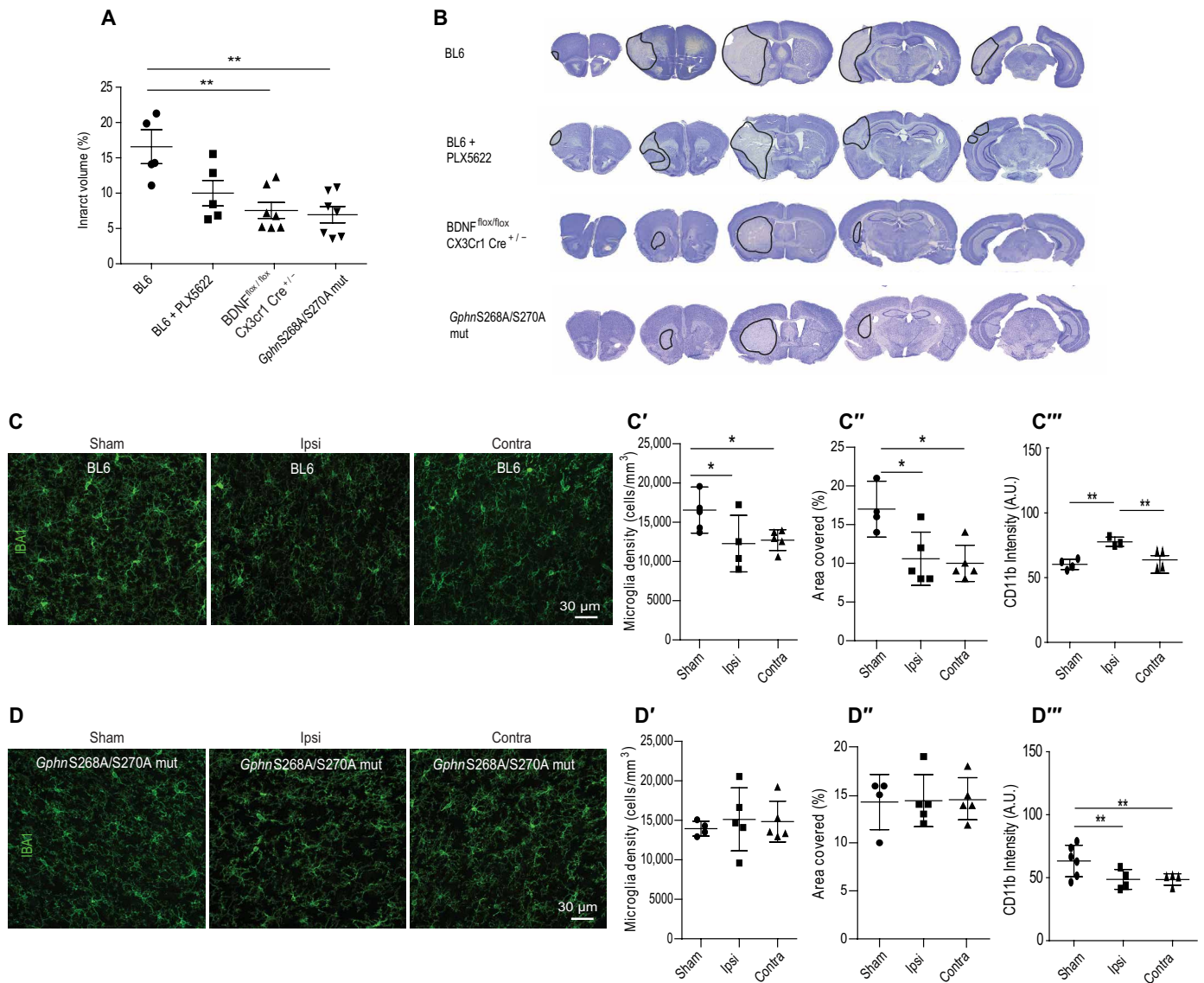
Fig. 8. *Gphn*S268A/S270A mutant mice show reduced neuroinflammation 24 hours following MCAO. (**A**) Quantification of infarct volume in BL6 WT, BL6 WT treated with PLX5622, BDNF$^{flox/flox}$/CX3CR1$^{ERT2Cre+/-}$, and *Gphn*S268A/S270A mutant mice at 24 hours following MCAO [one-way ANOVA, Brown-Forsythe test; $F_{3,15} = 8.9$; $P = 0.0028$]. **$P < 0.01$. (**B**) Example image of volumetric analysis from 24 hours after MCAO tissue sections from BL6 WT, BL6 WT treated with PLX5622, BDNF$^{flox/flox}$/CX3CR1$^{ERT2Cre+/-}$, and *Gphn*S268A/S270A mutant mice. Results expressed as means ± SD ($n = 5$ or more). (**C**) Example images of BL6 WT mice stained from sham or 24 hours after MCAO tissue for microglia markers IBA1 and CD11b (IBA1 shown). (**C'**) Quantification for microglia density in sham animals and ipsi- and contralateral sides of MCAO animals. *$P < 0.05$. (**C''**) Quantification microglia area covered using IBA1 staining from sham animals and ipsi- and contralateral sides of MCAO animals. *$P < 0.05$. (**C'''**) Quantification for CD11b intensity in sham animals and ipsi- and contralateral sides after MCAO animals. **$P < 0.01$. (**D**) Example images of *Gphn*S268A/S270A mutant mice stained from sham or 24 hours after MCAO tissue for microglia markers IBA1 and CD11b (IBA1 shown). (**D'**) Quantification for microglia density in sham animals and ipsi- and contralateral sides of MCAO animals. (**D''**) Quantification microglia area covered using IBA1 staining from sham animals and ipsi- and contralateral sides of MCAO animals. (**D'''**) Quantification for CD11b intensity in sham animals and ipsi- and contralateral sides after MCAO animals. Results expressed as means ± SD ($n = 5$ animals); *$P < 0.05$, **$P < 0.01$ (one-way ANOVA, Bonferroni multiple comparison test).

To understand whether GABAergic and/or glutamatergic transmission directly affected BDNF changes within microglia, we moved to BV2 microglia cell line. These are immortalized microglia cells that are comparable to microglia in vivo. We treated BV2 cells with vehicle control, GABA$_A$R antagonist bicuculline (BIC; 20 µM for 90 min), or glutamate receptor antagonists cyanquixaline and (2R)-amino-5-phosphonopentanoate [6-cyano-7-nitroquinoxaline-2,3-dione (CNQX) (20 µM) + AP5 (100 µM) for 90 min]. We performed WB analysis to measure changes in proBDNF and mBDNF levels after treatments (Fig. 9, D to D''). Quantification showed significant increase in both proBDNF and mBDNF after BIC treatment but not CNQX + AP5 treatment (Fig. 9, D and D'). This suggests that altered GABA could directly trigger BDNF production within microglia after MCAO. In addition, we used WB to assess for changes in total gephyrin protein and gephyrin phosphorylation within microglia after treatment with GABA$_A$R or glutamate
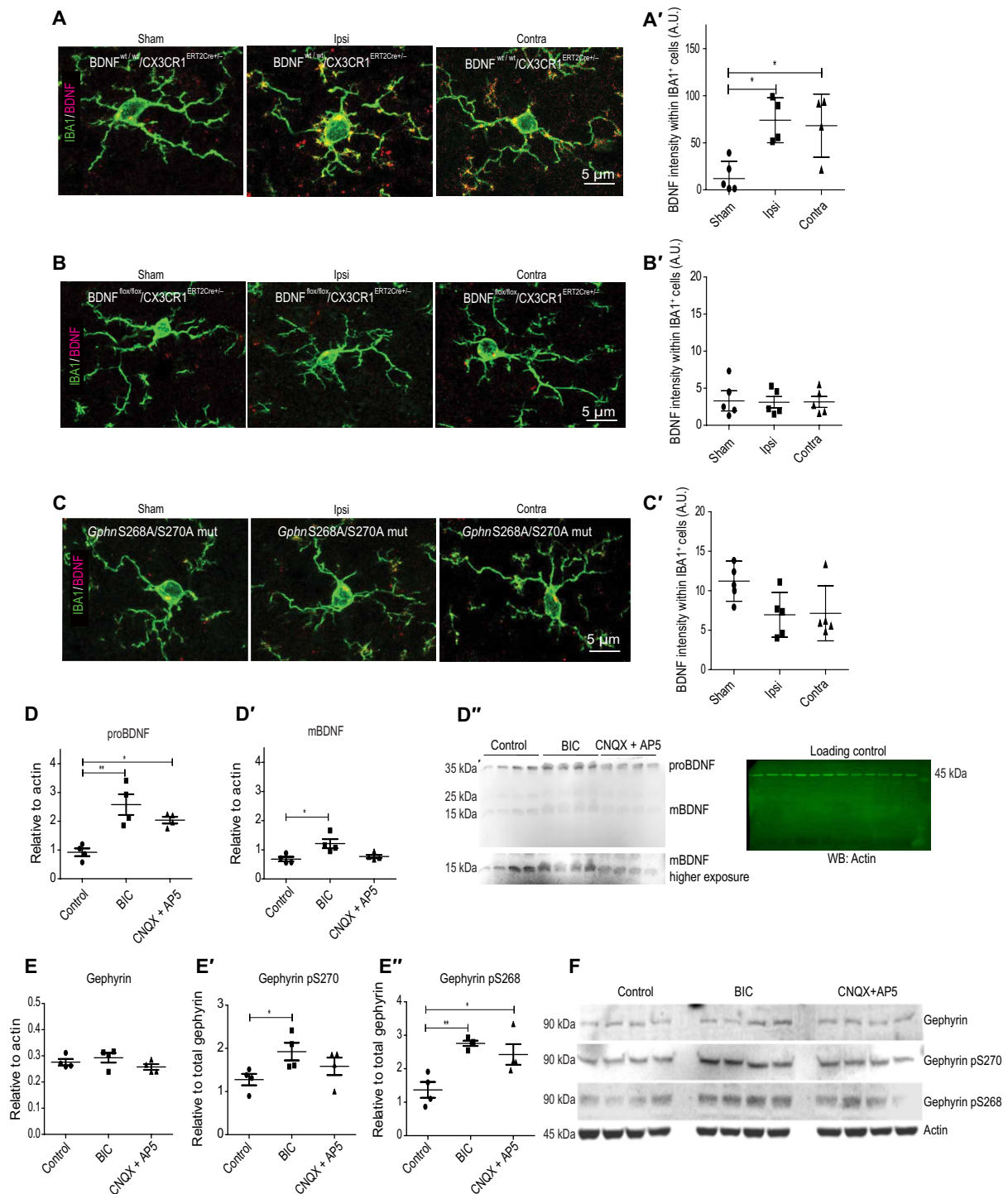
Fig. 9. *Gphn*S268A/S270A mutation affects BDNF levels in microglia after MCAO. (**A**) Example images from BDNF[wt/wt]/CX3CR1[ERT2Cre+/−] mice stained from sham or 24 hours after MCAO tissue for microglia markers IBA1 and BDNF (composite shown). (**A′**) Quantification for BDNF intensity within IBA1-positive cells in BDNF[wt/wt]/CX3CR1[ERT2Cre+/−] sham animals and ipsi- and contralateral sides of MCAO animals. *$P < 0.05$. (**B**) Example images from BDNF[flox/flox]/CX3CR1[ERT2Cre+/−] mice stained from sham or 24 hours after MCAO tissue for microglia markers IBA1 and BDNF. (**B′**) Quantification for BDNF intensity within IBA1-positive cells in BDNF[flox/flox]/CX3CR1[ERT2Cre+/−] sham animals and ipsi- and contralateral sides of MCAO animals. (**C**) Example images from GphnS268A/S270A mutant sham animals and ipsi- and contralateral sides of MCAO animals. (**C′**) Quantification for BDNF intensity within IBA1-positive cells in GphnS268A/S270A mutant sham animals and ipsi- and contralateral sides of MCAO animals. (**D** to **D″**) WB analysis for proBDNF and mBDNF in BV2 microglia cell line after treatment with BIC (20 μM) or CNQX (20 μM) + AP5 (100 μM) for 90 min. Blots with protein bands and actin loading control are shown on the right. *$P < 0.05$, **$P < 0.01$. (**E** to **E″**) WB analysis for total gephyrin, phospho-gephyrin at Ser[268], and phospho-gephyrin Ser[270] in BV2 microglia cell line after treatment with BIC (20 μM) or CNQX (20 μM) + AP5 (100 μM) for 90 min. *$P < 0.05$, **$P < 0.01$. (**F**) Blots showing the gephyrin protein bands and actin loading control ($n = 4$); *$P < 0.05$ (one-way ANOVA, Bonferroni multiple comparison test).

receptor antagonist. While total gephyrin level remained stable at 90 min after antagonist treatment, we found significant increase in gephyrin phosphorylation at Ser[268] and Ser[270] sites (Fig. 9, E and F). Together, our results confirm that microglia express gephyrin, proBDNF, and mBDNF. Furthermore, we identify that GABA$_A$Rs directly contribute to changes in proBDNF, mBDNF, and gephyrin phosphorylation changes within microglia.

Microglia have been implicated in the rapid engulfment and clearance of synapses following inflammatory brain pathology (39). To assess whether *Bdnf* gene deletion influenced microglia ramification after MCAO, we stained for IBA1 in BDNF[wt/wt]/CX3CR1[CreERT2+/−] and BDNF[flox/flox]/CX3CR1[CreERT2+/−] mice. It has been reported that macrophages infiltrate into the CNS only at day 4 following MCAO (40); therefore, IBA1-positive cells are likely to be resident microglial cells. We performed three-dimensional (3D) volume analysis of reconstructed microglia cells from ipsi- and contralateral hemispheres (Fig. 10A). Quantification showed a significant volume increase in the ipsilateral but not the contralateral hemisphere in BDNF[wt/wt]/CX3CR1[CreERT2+/−] mice, while there was no change in microglia volume in BDNF[flox/flox]/CX3CR1[CreERT2+/−] mice 24 hours after MCAO (Fig. 10A). Our data show significant hypertrophy, indicative of microglial activation, in the ipsilateral hemisphere of only BDNF[wt/wt]/CX3CR1[CreERT2+/−] mice. The lack of microglial activation in BDNF[flox/flox]/CX3CR1[CreERT2+/−] mice suggests that prevention of microglia BDNF release not only preserves synapses but also prevents alterations in microglia morphology.

Here, we demonstrate a direct link between gephyrin phosphorylation at Ser[268] and Ser[270] and BDNF changes within microglia after MCAO. Our results confirm that gephyrin phosphorylation regulates BDNF levels within microglia to initiate release and downstream signaling that ultimately lead to synapse loss following cerebral ischemia (see model in Fig. 10B).

DISCUSSION

This study reveals a direct connection between microglia, BDNF signaling, and gephyrin phosphorylation as a key pathway regulating tissue integrity and synapse loss after ischemic stroke. Preventing BDNF release from microglia or preventing gephyrin phosphorylation at Ser[268] and Ser[270] is equally protective against synapse loss within 24 hours after ischemic injury. Specifically, we demonstrate that (i) gephyrin in microglia regulates the release of proBDNF and mBDNF to act on p75[NTR] and TrkB receptors, respectively, and facilitate glutamatergic and GABAergic synapse loss after ischemia; (ii) ERK1/2 and GSK3β kinase phosphorylate gephyrin at Ser[268] and Ser[270] downstream of TrkB for GABAergic synapse down-regulation; (iii) in vivo microglia-specific *Bdnf* gene deletion or expression of gephyrin phospho-null S268A/S270A mutant protect against synapse loss at 24 hours after MCAO; (iv) *Gphn*S268A/S270A mutant mice prevent microglia activation and synapse loss at 24 hours after MCAO; (v) GABA$_A$R antagonists facilitate increase in proBDNF, mBDNF, and gephyrin phosphorylation within microglia, perhaps through the GABA$_A$Rs expressed in the microglia; and (vi) the mouse lines tested in our study consistently indicate similar changes within both ipsi- and contralateral hemispheres, which is rarely addressed in stroke studies. Together, microglia activation and BDNF secretion are tightly coupled to glutamatergic and GABAergic synapse integrity in our model of ischemia-induced brain injury.
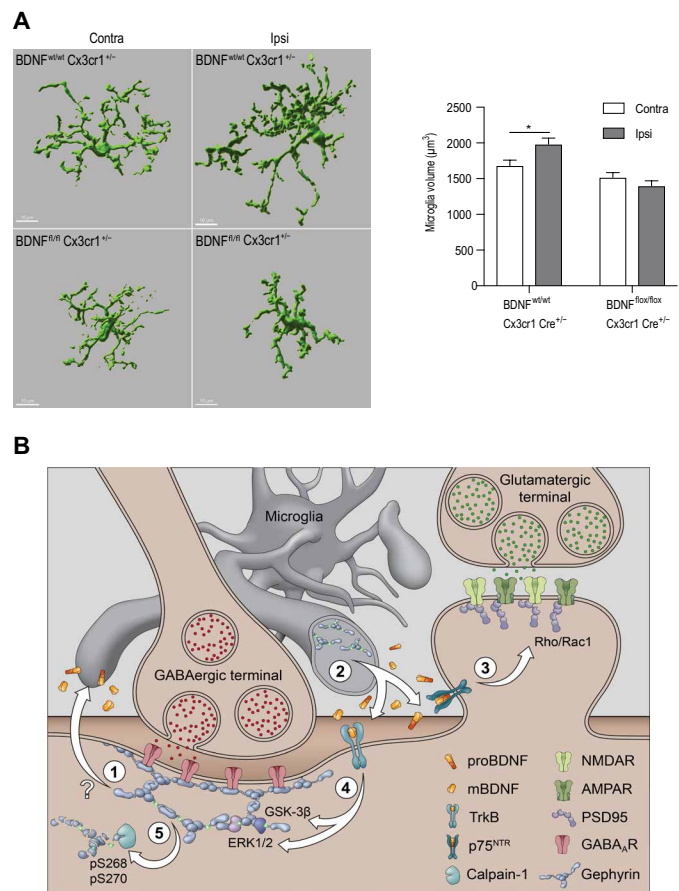
Fig. 10. Microglia volume change in BDNF[flox/flox]/CX3CR1[CreERT2+/−] mice after MCAO. (**A**) Example image of 3D volumetric analysis of IBA1-positive cells in BDNF[wt/wt]/CX3CR1[CreERT2+/−] mice and BDNF[flox/flox]/CX3CR1[CreERT2+/−] mice ipsi- and contralateral sides. Quantification of volume analysis in BDNF[wt/wt]/CX3CR1[CreERT2+/−] mice and BDNF[flox/flox]/CX3CR1[CreERT2+/−] mice ipsi- and contralateral sides. Data are shown as means ± SD (*n* = 5 animals); *$P < 0.05$. (**B**) Overview of pathway(s) interlinking inflammation, microglia gephyrin, and synaptic gephyrin to facilitate glutamatergic and GABAergic synapse loss at 24 hours after MCAO through proBDNF and mBDNF; (1) gephyrin phosphorylation at Ser[268]/Ser[270] at GABAergic postsynaptic sites and/or GABA-dependent gephyrin phosphorylation at Ser[268]/Ser[270] within microglia contribute to ischemia-induced synapse loss. GphnS268A/S270A mutant mice show reduced microglia hyper reactivity after MCAO and BV2 cells treated with BIC show increased gephyrin phosphorylation and elevated levels of proBDNF and mBDNF; (2) activated microglia release proBDNF and mBDNF to act on their cognate receptors p75[NTR] and TrkB respectively; (3) proBDNF via p75[NTR] activates RhoA/Rac1 pathway for actin remodeling and spine loss, triggering microglia-aided stripping of VGLUT terminals; (4) ERK1/2 and GSK3β pathways are activated downstream of TrkB receptors to phosphorylate gephyrin at Ser[268] and Ser[270] residues, respectively; (5) gephyrin phosphorylation at Ser[268] and Ser[270] leads to gephyrin scaffold loss via calpain-1 cleavage to facilitate GABA$_A$R internalization and microglia-aided displacement of GABAergic terminals. This mechanism outlines how excitatory and inhibitory synapses are lost at both ipsi- and contralateral sides 24 hours after ischemia.

GABAergic system in ischemia

Our results concur with previous observations in the gerbil where following transient cerebral ischemia (24 hours), GABA$_A$Rs are down-regulated (6). In mice, it was reported that tonic GABA currents are increased in the peri-infarct area 3 days after ischemia. An impairment in GABA transporter GAT3/GAT4 function was shown

to contribute toward up-regulation of extrasynaptic α5 and δ GABA$_A$R tonic current (41). In this study, we report a reduction in synaptic GABA$_A$R subunits α1, α2, and γ2 and also extrasynaptic α5 subunit expression at 24 hours after ischemia (Fig. 5 and fig. S4). In addition, we report that presynaptic GAD65/67 terminals are also significantly reduced at 24 hours after ischemia. Our data indicate that by stabilizing GABAergic synaptic and extrasynaptic transmission, one can reduce ischemic brain damage (Fig. 8A). It has also been reported that inverse agonists specific for α5 subunit–containing extrasynaptic GABA$_A$Rs administered 4 days after stroke promotes early stroke recover (41). Hence, it is conceivable that the increase in extrasynaptic GABA$_A$Rs observed at day 4 after ischemia is a homeostatic response to the early reduction in GABA and synaptic GABA$_A$Rs. The observed increase in gephyrin phosphorylation at Ser[268] and Ser[270] in BV2 cells upon BIC treatment could explain the neuroprotection observed in *Gphn*268A/S270A mutant mice at 24 hours after ischemia.

Postsynaptic scaffold stability after ischemia

In WT mice, 24 hours after MCAO gephyrin protein levels are reduced (fig. S3E); however, we observe no change in PSD95 clusters, as a proxy for glutamatergic postsynaptic sites (Fig. 5C). Previous studies have revealed that after ischemia, nNOS interaction with PSD95 stabilizes the protein at postsynaptic sites (29). Gephyrin has also been reported to interact with nNOS (42). However, it remains to be tested whether interaction with nNOS is influenced by ERK1/2 and GSK3β phosphorylation of gephyrin. It is possible that reduced gephyrin expression after MCAO might make more nNOS available for PSD95 interaction and stabilization. If neuroinflammation is the trigger for nNOS activation, then our data show reduced inflammation in *Gphn*S268A/S270A mutant mice and BDNF$^{flox/flox}$;CX3CR1$^{CreERT2+/−}$ cKO mice. Therefore, BDNF signaling could increase neuroinflammation by activating nNOS after ischemia.

proBDNF and mBDNF signaling regulates synapse down-regulation

At the neuromuscular junction, proBDNF and mBDNF elicit opposite effects by promoting axon retraction through activation of p75^{NTR} on presynaptic site or potentiate synapse through TrkB activation at the postsynaptic site, respectively. High-frequency neuronal activity controls the ratio of extracellular proBDNF/mBDNF by regulating the secretion of extracellular proteases, serving as a reward signal to stabilize synaptic contacts and strengthen neurotransmission (43) However, within hippocampal neurons, proBDNF has been reported to activate p75^{NTR} localized in dendritic spines of CA1 neurons and enhance NMDA Receptor 2B (GluN2B)–dependent long-term depression (44).

In the current study, we present evidence for proBDNF and mBDNF in glutamatergic and GABAergic synapse down-regulation after ischemia. p75^{NTR} lack intrinsic enzymatic activity and activate signal transduction pathway by associating with adaptor proteins that are distinct from TrkB signaling cascade (45). Consistent with this literature, our data show the specificity for proBDNF and p75^{NTR} signaling for spine down-regulation and mBDNF and TrkB for gephyrin regulation at GABAergic postsynaptic sites (Fig. 3 and fig. S2, E to H′). Our study has important implications. First, we uncover a synaptic plasticity function for proBDNF and p75^{NTR} in the ischemic brain, which is in marked contrast to its role in regulating

neuronal apoptosis. Second, our results show that TrkB and downstream pathways (ERK1/2 and GSK3β) specifically influence the stability of shaft synapse but not of spine synapses (Fig. 4).

Microglia as a source of BDNF in ischemia

Deletion of BDNF from specific subpopulations of neurons has revealed that both presynaptic and postsynaptic BDNF contributes to specific aspects of long-term potentiation (LTP). For example, presynaptic BDNF was documented to increase the strength of LTP, while postsynaptic BDNF facilitates LTP maintenance (46). In addition, BDNF release from dendritic spines can activate N-methyl-D-aspartate and TrkB receptors within the same release site to influence structural plasticity. At GABAergic terminals, time duration of exogenous BDNF exposure has opposite effects on GABA$_A$R and gephyrin clustering. In hippocampal neuron culture, short-term (5-min) BDNF application inhibits GABA$_A$R internalization through phosphoinositide-3 kinase and protein kinase C pathways (47). However, long-term (90-min) BDNF application reduces GABA$_A$R and gephyrin clustering (48). Presynaptically, BDNF regulates GAD65 mRNA expression through the recruitment of ERK pathway, leading to CREB activation.

To add to this complexity, BDNF is not only found in neurons but also expressed in both astrocytes and microglia (30, 49). Within the spinal cord circuit, BDNF activates TrkB in lamina I neurons to down-regulate KCC2 (chloride potassium symporter), thereby increasing intracellular chloride concentration and reversing GABAergic inhibition to cause neuronal depolarization (35). The resulting hyperexcitability of neurons contributes to mechanical hypersensitivity. Microglia-specific *Bdnf* knockout reduces perineural invasion (PNI)–induced pain (50). In the current study, we report microglia as the major source of BDNF after ischemia for glutamatergic and GABAergic synapse regulation. We observed elevated proBDNF in PLX5622-treated mice under sham condition, which suggests that microglia ablation at baseline could trigger proBDNF synthesis from other cell types as compensatory mechanism (fig. S6A′). proBDNF levels reduce significantly in PLX5622-treated animals after MCAO, indicating that microglia play a pivotal role in de novo BDNF synthesis; we also do not know how different metalloproteases are affected after microglia depletion. The release of BDNF from microglia has been linked to purinergic receptor P2X4R activation, causing disinhibition of pain-transmitting spinal lamina I neurons (51, 52). Using BV2 cells, we uncover that GABA$_A$R antagonist can specifically increase the expression of proBDNF and mBDNF and increase gephyrin phosphorylation at Ser[268] and Ser[270] residues. Hence, it is possible that, at 24 hours after ischemia, transient reduction in GABA triggers BDNF protein synthesis and release from microglia.

Gephyrin phosphorylation influences microglia activation

During acute ischemic stroke, natural killer (NK) cells infiltrate peri-infarct areas of the brain to promote inflammation (e.g., microglia activation) and neuronal damage. Depletion of NK cells within the first 12 hours after MCAO attenuates neurological deficits and infarct volume (53). Here, we report that microglia depletion using PLX5622 (fig. S5) and *Bdnf* gene deletion specifically from microglia (fig. S4) prevent glutamatergic and GABAergic synapse loss and reduce the extent of infarct volume (Fig. 7A) after ischemia. Hence, it is possible that NK cells influence infarct development through GABA release for microglia activation and local BDNF release to trigger glutamatergic and GABAergic synapse loss. Furthermore, in

addition to activation of microglia, we uncover activation of ERK1/2 and GSK3β pathways (Fig. 5, G to I) 24 hours after ischemia. As a direct target of ERK1/2 (26) and GSK3β (25), gephyrin phosphorylation at Ser^{268} and Ser^{270} sites are significantly increased after ischemia, while total gephyrin level is decreased (Fig. 5, J to J‴). Stabilization of gephyrin clusters through the expression of S268A/S270A mutant in hippocampal slice culture selectively prevents GABAergic synapse loss after ischemia (Fig. 4, H and I). In GphnS268A/S270A mutant mice, both glutamatergic and GABAergic synapse loss can be prevented (Fig. 6). This suggests that gephyrin phosphorylation changes both within microglia and neurons might contribute differentially to ischemia induced inflammation and synapse loss. In addition, given the lack of vasculature changes in slice cultures, it is expected that we observe divergence of data between organotypic slice cultures and GphnS268A/S270A mutant mice.

We reveal a link between gephyrin phosphorylation at Ser^{268} and Ser^{270}, microglia activation, and BDNF secretion (see model in Fig. 10B). Within this model, GABAAR antagonism, reduced GABA, or a signal originating at GABAergic postsynaptic sites would activate microglia to synthesize and release proBDNF and mBDNF for downstream signaling after MCAO. This is based on our data showing that BDNF protein levels do not change after MCAO in Gphn268A/S270A mutant mice, which suggests that gephyrin phosphorylation within microglia and its scaffold stability within GABAergic postsynaptic compartment control microglia activation. The glutamatergic spine synapse collapse through $p75^{NTR}$ signaling and GABAergic synapse down-regulation via gephyrin phosphorylation at Ser^{268} and Ser^{270} could facilitate microglia-aided stripping of VGLUT and VGAT terminals. It has been reported that microglia physically displace GABAergic presynaptic terminals after LPS-induced inflammation (54). Together, our data identify the mechanistic basis for silencing neurotransmission at the initial 24 hours after MCAO.

MATERIALS AND METHODS
Ethics statement
All animal handling procedures were carried out consistent with guidelines set by the Canadian Council on Animal Care, the European Community Council Directives of 24 November 1986 (86/609/EEC) and approved by the cantonal veterinary office of Zurich (ZH219/15). All procedures were approved by the Animal Resource Committee of the School of Medicine at McGill University and are outlined in McGill University Animal Handling Protocol no. 5057.

Hippocampal slice cultures and OGD
We have chosen to study the hippocampus as it has a unique unidirectional network that is preserved within organotypic cultures (55), making it an ideal candidate to study microcircuitry remodeling. Organotypic hippocampal slices were prepared using the roller tube method, as previously described (55) with transgenic mice expressing membrane-targeted MARCKS (myristoylated alanine-rich protein kinase C substrate)–enhanced GFP under the Thy-1 promoter in a subpopulation of CA1 cells. We used an established model of OGD as a model of ischemia (56); briefly, mature organotypic hippocampal slices were placed in a glass dish containing glucose-free Tyrode's solution [137 mM NaCl, 2.7 mM KCl, 2.5 mM CaCl₂, 2 mM MgCl₂, 11.6 mM NaHCO₃, and 0.4 mM NaH₂PO₄ (pH 7.4)] containing 2 mM 2-deoxyglucose, 3 mM sodium azide, and 8 mM

sucrose for 4 to 5 min and were then returned to culture medium for 90 min, 24 hours, or 1 week. Control slices were exposed to Tyrode's solution [137 mM NaCl, 2.7 mM KCl, 2.5 mM CaCl₂, 2 mM MgCl₂, 11.6 mM NaHCO₃, 0.4 mM NaH₂PO₄, and 5.6 mM glucose (pH 7.4)] for 4 to 5 min and returned to culture medium.

Mouse lines
All procedures fulfilled the ARRIVE (Animal Research: Reporting of In Vivo Experiments) guidelines on experimental design, animal allocation to different experimental groups, blinding of samples to data analysis, and reporting animal experiments. The GphnS268A/S270A mutant mouse was generated using CRISPR-Cas9 (Cyagen, USA) in BL6 background. These mutant mice develop normally and breed with Mendelian ratio. Heterozygous breedings were used to generate GphnS268A/S270A homozygous mutant mice; however, control C57Bl6/J-Crl1 mice were purchased from Charles River Laboratories (Germany). B6.129P2(C)-Cx3cr1tm2.1(cre/ERT2) (stock no. 020940) (57) mice and Bdnftm3Jae or $BDNF^{Tg}$ (stock no. 004339) (58) were obtained from the Jackson Laboratory, and heterozygous breeding pairs were set up to generate $BDNF^{wt/wt}/CX3CR1^{ERT2Cre+/-}$ and $BDNF^{flox/flox}/CX3CR1^{ERT2Cre+/-}$cKO lines. We compared results within same genotypes. The mice were injected (intraperitoneally) on four consecutive days with tamoxifen dissolved in corn oil (H-6278, Sigma-Aldrich; 1 mg/day) to induce Cre expression at 4 weeks, followed by sham or MCAO surgery at 8 to 9 weeks of age. Animals were randomly assigned, and both genders were used for both conditions. The PLX5622 treatment for microglia depletion followed the recommended company dose (1200 mg of active form of PLX5622/kg of chow).

MCAO model
WT C57Bl6/J-Crl1 mice were purchased from Charles River Laboratories (Germany), and the GphnS268A/S270A mutant, $BDNF^{flox/flox}/CX3CR1^{ERT2Cre+/-}$, were bred in house. At 4 weeks, age animals were randomly allocated to groups. The transient occlusion of the middle cerebral artery was conducted at 8 to 9 weeks age using the filament model as described previously (59). Briefly, anesthesia was induced using 3% isoflurane in an oxygen/air (1:4) mixture and maintained at 2% isoflurane. The area around the neck was shaved and disinfected, and an incision was made along the midline. The common and the external carotid artery were isolated and ligated. A silicon rubber filament (lot 701956RE, Doccol, USA) was inserted into the internal carotid artery to block the middle cerebral artery. The filament remained in place for 30 min before reperfusion was allowed by withdrawing it. During occlusion, the mouse was placed in a preheated (30°C) recovery box and allowed to recover from anesthesia. After reperfusion, the internal carotid artery was ligated to prevent bleeding, and the wound was sutured. Sham operation involved identical surgical procedures, but the filament was immediately withdrawn after insertion. A total volume of 500 µl of buprenorphine (0.03 mg/g) with saline was injected after surgery and consecutive after 4 and 8 hours subcutaneously. The mouse was kept for 2 hours in the recovery box and then placed back into its home cage. Mashed food and food pellets were placed on the cage bottom to encourage food uptake. The described lesion paradigm caused an extensive damage to the unilateral basal ganglia and the adjacent neocortex. For clinical scoring, mice were examined for forelimb flexion and body posture maintenance using the Bederson score (as described in www.ahajournals.org/doi/pdf/10.1161/01. STR.17.3.472). Animals were excluded from the studies when they fulfilled one of the following criteria: prolonged surgery time

(>15 min); no reflow after filament withdrawal; clinical scoring of 0; and seizures during/after MCAO or dead before experimental end point. A total of seven animals were excluded (three due to clinical scoring of 0 following MCAO and four due to seizures during/after MCAO).

Cresyl violet staining

Cresyl violet staining was performed 24 hours after of reperfusion, and infarct volume was assessed as percentage of the affected hemisphere. Five 20-μm-thick coronal sections taken at bregma +2.8, +1.54, +0.14, −1.94, and − 4.6 mm were stained with cresyl violet using vendor protocol and later digitalized using a Zeiss Axio Scan. Z1 at ×5 magnification, and lesions were determined using ZEN software (Zeiss). The person analyzing was blinded to the treatment groups. Cerebral lesion volume was calculated summing up the volume of each section while corrected for oedema (group numbers > 4).

Immunofluorescence and confocal microscopy
Hippocampal organotypic slices

Ninety minutes after OGD induction, hippocampal slices were fixed for 1 hour at room temperature in 4% paraformaldehyde (PFA) in 0.1 M phosphate buffer (PB) (pH 7.4). Slices were then washed five times in 0.1 M PB, permeabilized in 0.4% Triton X-100, and blocked with 1.5% heat-inactivated horse serum overnight at 4°C. Anti-gephyrin (1:500; Synaptic Systems) was incubated for 5 days at 4°C in permeabilizing buffer and washed five times with 0.1 M PB containing 1.5% heat-inactivated horse serum. Slices were incubated for 3 hours at room temperature with 1:250 anti-mouse DyLight 650 (Jackson ImmunoResearch, Burlington, ON, Canada) secondary antibody diluted in 0.1 M PB containing 1.5% heat-inactivated horse serum. Following washing five times with 0.1 M PB containing 1.5% heat-inactivated horse serum, slices were mounted with fluorescent mounting medium (Dako, Mississauga, ON, Canada) onto microscope slides.

Slices were imaged using a Leica TCS SP2 scan head (Leica Microsystems) on a Leica DM6000 B upright microscope, equipped with HCX PL APO 63× numerical aperture (NA) 1.4 oil immersion objective using a 543-nm HeNe laser line. Image stacks were collected at $Z = 0.3$ μm and averaged two to three times to improve signal-to-noise ratio. For quantification, image stacks were obtained with identical parameters (laser intensity, filters, pinhole size, photomultiplier tube gain, and offset). Representative images are maximum intensity projections of five sections from each stack.

Immunohistochemical imaging of brain slices

Twenty-four hours following MCAO, postnatal day 60 to 70 (male or female) mice were anesthetized by intraperitoneal pentobarbital injection (Nembutal; 50 mg/kg) and perfused transcardial with ice-cold oxygenated artificial cerebrospinal fluid (pH 7.4) (60) for 2 min. Brains were immediately fixed in 4% PFA for 3 hours at 4°C. After rinsing in phosphate-buffered saline (PBS), brains were incubated in 30% sucrose (in PBS) at 4°C overnight. Coronal sections (45 μm in thickness) were cut from frozen blocks using a sliding microtome (HM400, Microm) and stored at −20°C in antifreeze solution. After three times of 10-min washes in tris-Triton solution [50 mM tris, 150 mM NaCl, and 0.05% Triton X-100 (pH 7.4)], sections were incubated in primary antibody solution [50 mM tris, 150 mM NaCl, 0.4% Triton X-100, and 2% normal goat serum (pH 7.4)] at 4°C overnight. Primary antibodies are listed in Table 1. Sections were washed three times for 10 min in tris-Triton solution and incubated in secondary antibody solution [50 mM tris, 150 mM NaCl, 0.05% Triton X-100, and 2% normal goat serum (pH 7.4)] for 1 hour at room temperature with secondary antibodies raised in goat. All secondary antibodies used were diluted 1:500. Antibodies conjugated to Alexa Fluor 488 and Alexa Fluor 647 were purchased from Invitrogen, while antibodies conjugated to Cy3 were purchased from Jackson ImmunoResearch Laboratories. Sections were washed three times for 10 min in tris-Triton solution and mounted on gelatin-coated slides using Fluorescence Mounting Medium (Dako). Z-stack images (four optical sections, 0.75-μm step size) were recorded of all sections using confocal laser scanning microscopy (LSM 700, Carl Zeiss). Images were taken using a 40× objective with an NA of 1.4 and pixel size of 112 nm^2. Three juxtaposed images of the motor cortex L2/3 were taken on the ipsi- and contralateral hemispheres. To reduce variability, multiple images were captured from three sections per mouse, and a total of four to five mice were analyzed per condition/genotype. Cluster density values were averaged from these sections. All imaging parameters were kept constant between MCAO and sham animals. For cluster analysis, a custom Python script using the ImageJ image processing framework was used. The script can be used as a plugin and is openly available on a GitHub repository (https://github.com/dcolam/Cluster-Analysis-Plugin). Representative example images were processed using ImageJ. Statistical tests were performed using Prism software (GraphPad) using five mice per group.

Microglia analysis

Iba1 staining was acquired using a spinning-disk confocal microscope (Nikon Ti2 coupled to Yokogawa CSU-W1 confocal scanning unit) with an Omicron modified Light HUB+ laser emitting at 488 nm and a CFI Plan Apochromat Lambda 60× oil objective (NA, 1.40; W.D., 0.13 mm). 3D stack images of 25.5 μm were acquired with a z step of 0.3 μm in layer II/III of the motor cortex (two to three slices per animal and five animals per group). For the microglia density analysis, individual microglial cells were counted in Fiji, through colocalization of the Iba1 and 4′,6-diamidino-2-phenylindole staining in 3D and the "Analyze Particles" function. The mean intensity and area covered by the Iba1 signal were analyzed on the maximum intensity projection of the stack in Fiji.

Imaris software (Bitplane, Switzerland) was used for reconstruction of MCAO BDNF$^{wt/wt}$/CX3CR1$^{CreERT2+/−}$ and BDNF$^{flox/flox}$/CX3CR1$^{CreERT2+/−}$ cells. 3D rendering of microglial volume was based on Iba1 immunoreactivity, applying recorded algorithms with fixed thresholds for Iba1 signal intensity. Morphometric values were extracted per individual cells (BDNF$^{wt/wt}$/CX3CR1$^{CreERT2+/−}$: contra, $n = 68$; ipsi, $n = 72$; BDNF$^{flox/flox}$/CX3CR1$^{CreERT2+/−}$: contra, $n = 82$; ipsi, $n = 94$).

Dendrite reconstructions, spine quantification, cluster quantification

3D confocal stacks were deconvolved with Huygens Essentials software (Scientific Volume Imaging, Hilversum, The Netherlands) using a full maximum likelihood extrapolation algorithm. Stacks were then imported and rendered using the Surpass function in Imaris software (Bitplane). Experimenter was blinded to conditions and treatment groups; spines were manually counted; and using the ratio of the diameter and length of the head and neck of spines, it was possible to distinguish between stubby, mushroom, and thin subtypes of dendritic spines. These classifications were based on established criteria. Last, n values for spine analysis represent ~75 to 100 μm of dendrite from one to two cells imaged from each slice.

Table 1. Antibody list. GFAP, glial fibrillary acidic protein.

Target	Host species	Dilution	Catalog no.	Company/origin
Antibodies used for immunohistochemistry				
GABA$_A$R γ2	Guinea pig	1:2000	–	Homemade
GABA$_A$R α5	Guinea pig	1:3000	–	Homemade
GAD65/67	Rabbit	1:1000	GC 3008	Affiniti
VGLUT1	Guinea pig	1:1000	135 304	Synaptic Systems
PSD95	Mouse	1:1000	73-028	NeuroMap
GFAP	Mouse	1:2000	MAB360	Millipore
IBA1	Rabbit	1:1000	019-19741	Wako
CD11b	Rat	1:50	550282	BD Pharmingen
mBDNF N-9	Mouse	1:100	BDNF #9	DSHB
p75^{NTR}	Rabbit	1:200	AB-NO1	Advanced Targeting System
proBDNF #B240	Mouse	1:200		Philip Barker
Antibodies used for WB				
GABA$_A$R α1	Rabbit	1:600	–	Homemade
GABA$_A$R α2	Rabbit	1:1000	–	Homemade
Gephyrin	Mouse	1:1000	147 111	Synaptic Systems
Gephyrin pS268	Rabbit	1:500	–	Homemade
Gephyrin pS270	Rabbit	1:500	–	Homemade
GSK3β	Rabbit	1:1000	ab124661	Abcam
ERK1/2	Rabbit	1:4000	9102S	Cell Signaling Technology
Phospho-Erk1/2 (Thr^{202}/Tyr^{204})	Rabbit	1:4000	9101	Cell Signaling Technology
BDNF	Rabbit	1:3000	Ab108319	Abcam
BDNF	Mouse	1:3000	Ab327	Icosagen
Actin	Mouse	1:10,000	MAB1501	Millipore

The number and volume of gephyrin clusters were quantified using the Spot function of Imaris software, which differentiates puncta based on the fluorescence intensity.

Electrophysiological recordings and analysis
Slices were transferred into a temperature-controlled chamber (25°C) mounted on an upright microscope (DM LFSA, Leica Microsystems) and continuously perfused with external solution [137 mM NaCl, 2.7 mM KCl, 2.5 mM, CaCl$_2$, 2 mM MgCl$_2$, 11.6 mM NaHCO$_3$, 0.4 mM NaH$_2$PO$_4$, and 5.6 mM glucose (pH 7.3)]. Patch recording electrodes were pulled from borosilicate glass (GC150TC, Clark Instruments, Old Sarum, Salisbury, UK). All electrophysiological recordings were made using an Axopatch 200A amplifier (Molecular Devices, Sunnyvale, CA, USA).

AMPA-mediated mEPSCs were gathered from whole-cell voltage-clamp recordings of CA1 pyramidal neurons obtained at 25°C using electrodes with resistances of 4 to 5 megohms and filled with intracellular solution containing 120 mM K-gluconate, 1 mM EGTA, 10 mM Hepes, 5 mM Mg–adenosine 5′-triphosphate (ATP), 0.5 mM Na–guanosine 5′-triphosphate (GTP), 5 mM NaCl, 5 mM KCl, 10 mM phosphocreatine, 295 mOsm, and pH adjusted with KOH to 7.3. mEPSCs were recorded at −60 mV and in the presence of 1 μM tetrodotoxin (TTX), 15 μM 3-[(R)-2-carboxypiperazin-4-yl]-propyl-1-phosphonic acid (CPP), 100 μM picrotoxin, and 1 μM CGP55845 in the external Tyrode's solution. Access resistance was monitored with brief test pulses at regular intervals (2 to 3 min) throughout the experiment. Access resistance was usually 10 to 13 megohms, and data were discarded if the resistance deviated more than 10% through the course of the experiment. Series resistance of the access pulse and decay time was also used for the calculation of total membrane capacitance. After the holding current had stabilized, data were recorded at a sampling frequency of 10 kHz and filtered at 2 kHz for 10 to 15 min.

GABA$_A$R-mediated mIPSCs were gathered from whole-cell voltage-clamp recordings of CA1 pyramidal neurons obtained at 25°C using electrodes with resistances of 4 to 5 megohms and filled with intracellular solution containing 140 mM CsCl, 4 mM NaCl, 0.5 mM CaCl$_2$, 10 mM Hepes, 5 mM EGTA, 2 mM QX-314, 2 mM Mg-ATP, 0.5 mM Na-GTP, 290 mOsm, and pH adjusted with CsOH to 7.36. mIPSCs were recorded at −60 mV and in the presence of 1 μM TTX, 25 μM CPP, 5 μM CGP55845, 5 μM CNQX, and 0.3 μM strychnine in external Tyrode's solution. Access resistance was monitored with brief test pulses at regular intervals (2 to 3 min) throughout the experiment. After the holding current had stabilized, data were recorded at a sampling frequency of 10 kHz and filtered at 2 kHz for 10 to 15 min.

All mEPSCs and mIPSCs were detected offline using the Mini Analysis software (Synaptosoft, Decatur, GA, USA). The amplitude

threshold for mEPSC and mIPSC detection was set at four times the root mean square value of a visually event-free recording period. From every experiment, 5 min of stable recording was randomly selected for blinded analysis of amplitude and IEI. The data obtained were then used to plot cumulative histograms with an equal contribution from every cell. For statistical analysis, data were averaged for every single cell. It should be noted that the amplitude analysis was conducted only on single mEPSCs and mIPSCs that did not have subsequent events occurring during their rising and decaying phases. For frequency analysis, all selected events were considered.

Pharmacological treatments

To scavenge BDNF, slices were treated with TrkB-Fc (R&D Systems, Minneapolis, MN, USA), a fusion protein in which the BDNF binding site of the TrkB receptor replaces the Fc fragment of a human immunoglobulin G1 antibody. We found that TrkB-Fc treatment to hippocampal cultures for 24 hours down-regulated TrkB receptor phosphorylation. TrkB-Fc was diluted in culture medium at a final concentration of 10 μg/ml, and treatment began immediately following induction of OGD. ERK activation was inhibited using 30 μM MEK inhibitor PD98059 (Tocris Bioscience, ON, Burlington, Canada), and GSK3β activity was inhibited using 25 μM GSK3β-IX (Tocris Bioscience). PD98059 and GSK3β-IX were diluted in dimethyl sulfoxide (Invitrogen) and treatment began overnight before OGD induction, removed during induction, and continued for 90 min after. Control sister cultures were treated with control culture medium containing dimethyl sulfoxide only. The following function blocking antibodies were used: anti-p75[NTR] (1:200; gift from P. Barker, McGill University, Montreal, QC, Canada; Rex antibody, for more information, see (61)); anti-proBDNF (1:200; gift from P. Barker, McGill University, Montreal, Canada); and anti-mBDNF (1:100; N-9, Developmental Studies Hybridoma Bank, University of Iowa, IA, USA). Function blocking antibody treatment began 2 hours before OGD induction, removed during induction, and continued for 90 min after. Either recombinant proBDNF (100 ng/ml; Alomone) or recombinant BDNF (100 ng/ml; PrepoTech) was added to organotypic hippocampal cultures for 90 min before assessing changes in gephyrin by immunohistochemistry and spine number.

Biolistic gene transfection

Cartridges were prepared according to the manufacturer's protocol (Helios Gene Gun, Bio-Rad). Briefly, 15 mg of gold particles (1 μm in diameter) were first coated with 0.05 M spermidine. Fifteen micrograms of plasmid DNA expressing tdTomato and 45 μg of gephyrin$_{WT}$-GFP or dephosphorylation mutant gephyrin-GFP S268A/S270A (gephyrin$_{S268A/S270A}$-GFP) were made. Plasmids were then precipitated onto the particles by adding CaCl$_2$. The coated particles were resuspended into 100% ethanol and infused into Tefzel tubing, which was then coated with the particles. Coated tubing was cut into 1.27-cm cartridges, which were then transfected into mature organotypic slice cultures by shooting at a distance of 2 cm with a pressure of 200 psi through a nylon mesh. Following 48 hours, slices that expressed target plasmids in CA1 pyramidal neurons were processed with OGD or control Tyrode's solution.

Western blotting

Twenty-four hours following MCAO, mice were killed by decapitation, and brains were dissected on ice. The ipsi- and contralateral cortices were immediately transferred to lysis buffer [50 mM tris (pH 7.6), 150 mM NaCl, 1% Triton X-100, and cOmplete Mini

Protease Inhibitor Mixture (Roche)]. The cortices were homogenized and incubated on ice for 1 hour. Lysates were centrifuged at 20,000 rpm for 30 min at 4°C, and supernatants were stored at −80°C. Samples were run on tris-glycine polyacrylamide gels, and proteins were transferred to polyvinylidene difluoride membranes. Primary antibodies (see Table 1) were incubated in tris-buffered saline with 0.05% Tween 20 (TBST), including 5% Western Blocking Solution (Roche) overnight at 4°C. Membranes were washed five times for 5 min in TBST. Horseradish peroxidase (HRP)–coupled donkey secondary antibodies (1:30,000) and fluorescent coupled donkey secondary antibodies (1:20,000) were incubated for 30 min at room temperature, and membranes were washed again five times for 5 min in TBST. Fluorescent signals were captured using the Odyssey CLx Imager. SuperSignal West Pico Chemiluminescent substrate (Thermo Fisher Scientific) was applied to visualize HRP-labeled antibodies and developed using the FUJIFILM Luminescent Image Analyzer LAS-1000 plus & Intelligent Dark Box II (FUJIFILM). Images were analyzed using ImageJ, and statistical tests were performed using Prism software (GraphPad) using a minimum of four mice per group. WB membrane stripping was performed for p-ERK1/2 and ERK1/2 antibodies using a mild stripping protocol from Abcam. Briefly, membranes were incubated twice for 5 to 10 min with mild stripping buffer [200 mM gylcine, 20 mM SDS, and 0.01% Tween 20 (pH 2.2)], followed by two times 10-min incubation with PBS and two times 5-min incubation with TBST. Efficiency of stripping was checked by incubating with chemiluminescent detection. When stripping was judged satisfactory, the membranes were rinsed and incubated with primary antibody.

BV2 cell culture for WB analysis

BV2 cells were cultured in T75 cell culture flasks using Dulbecco's modified Eagle's medium: D-glucose and L-glutamine (4.5 g/liter), with pyruvate (#41966029, Gibco), 10% fetal bovine serum (#10437028, Gibco), 25 mM Hepes buffer solution (#15630056, 1M, Gibco), 1% gentamicin (#15710049, Gibco), and 1% fungizone/amphotericin B (#15290018, Gibco). The medium was changed every 2 to 3 days while in culture. The confluent cells in T75 flask were seeded on six-well plate, ~150 μl of cell suspension, and 2 ml of medium and grown to confluence. The cells were rinsed in PBS without MgCl$_2$ (#18912014, Gibco) before lysis in 150 μl of EBC buffer with cOmplete Mini, EDTA-free (#11836170001, Sigma-Aldrich). The lysis was performed for 20 min on shaker in 4°C. The cell debris was removed centrifugation at 200,000 rpm for 20 min at 4°C. The supernatant was transferred five times directly to SDS sample buffer and boiled. Six-well dishes were treated with BIC (20 μM) and CNQX (20 μM) + AP5 (100 μM) for 90 min before whole-cell lysate preparation.

Statistical analysis

An a priori power analysis was conducted and the significance of our results confirmed with the MCAO surgery procedure (Fig. 5). Combined with type 1 error set to 0.05 and power set to 0.8 (1 beta error), we determined the effect size with a group size of 5. These indicated an interindividual variation (SD) of 10 to 15%. We used multiple group comparison test (Bonferroni) to make maximal number of comparisons between groups.

For the slice culture comparison, we performed two-way analysis of variance (ANOVA) and independent t tests on the following figures: Fig. 2 (B, D, E, F, F′, G, and G′), Fig. 3 (B, C, D, F, G, and H), and Fig. 4 (B, C, D, G, H, and I). The t tests were performed to

confirm significance between conditions as two-way ANOVA and post hoc test do not cover all the comparisons of our interest. These t test P values are unprotected; therefore, we adjusted them using Bonferroni correction (e.g., if the set of the data is compared five times, then we need to multiply the P value by 5). The listed significant comparisons all have protected P values by Bonferroni posttest: *$P < 0.05$; **$P < 0.01$; ***$P < 0.001$.

Comparison between two groups was made using two-tailed independent Student's t test. Comparisons between multiple groups and treatments were made using two-way ANOVA with post hoc Bonferroni multiple comparison test. Comparisons between multiple groups were made using one-way ANOVA. Cumulative probability plots were compared using Kolmogorov-Smirnov test for probability distributions. Results are expressed as means ± SD.

SUPPLEMENTARY MATERIALS
Supplementary material for this article is available at https://science.org/doi/10.1126/sciadv.abj0112

View/request a protocol for this paper from *Bio-protocol*.

REFERENCES AND NOTES

1. E. S. Donkor, Stroke in the 21st century: A snapshot of the burden, epidemiology, and quality of life. *Stroke Res Treat*. **2018**, 1–10 (2018).
2. R. Brouns, P. P. D. Deyn, The complexity of neurobiological processes in acute ischemic stroke. *Clin Neurol Neurosur*. **111**, 483–495 (2009).
3. S. E. Lakhan, A. Kirchgessner, M. Hofer, Inflammatory mechanisms in ischemic stroke: Therapeutic approaches. *J. Transl. Med*. **7**, 97 (2009).
4. B. C. V. Campbell, D. A. D. Silva, M. R. Macleod, S. B. Coutts, L. H. Schwamm, S. M. Davis, G. A. Donnan, Ischaemic stroke. *Nat. Rev. Dis. Primers*. **5**, 70 (2019).
5. S. Zhang, J. Boyd, K. Delaney, T. H. Murphy, Rapid reversible changes in dendritic spine structure in vivo gated by the degree of ischemia. *J. Neurosci*. **25**, 5333–5338 (2005).
6. B. Alicke, R. D. Schwartz-Bloom, Rapid down-regulation of gabaa receptors in the gerbil hippocampus following transient cerebral ischemia. *J. Neurochem*. **65**, 2808–2811 (1995).
7. S.-J. Yu, K.-Y. Tseng, H. Shen, B. K. Harvey, Y. Wang, Local administration of AAV-BDNF to subventricular zone induces functional recovery in stroke rats. *Plos One*. **8**, e81750 (2013).
8. W.-R. Schäbitz, T. Steigleder, C. M. Cooper-Kuhn, S. Schwab, C. Sommer, A. Schneider, H. G. Kuhn, Intravenous brain-derived neurotrophic factor enhances poststroke sensorimotor recovery and stimulates neurogenesis. *Stroke* **38**, 2165–2172 (2007).
9. J. Yang, L. C. Harte-Hargrove, C.-J. Siao, T. Marinic, R. Clarke, Q. Ma, D. Jing, J. J. Lafrancois, K. G. Bath, D. Ballon, F. S. Lee, H. E. Scharfman, B. L. Hempstead, ProBDNF negatively regulates neuronal remodeling, synaptic transmission, and synaptic plasticity in hippocampus. *Cell Rep*. **7**, 796–806 (2014).
10. J.-I. Tanaka, Y. Horiike, M. Matsuzaki, T. Miyazaki, G. C. R. Ellis-Davies, H. Kasai, Protein synthesis and neurotrophin-dependent structural plasticity of single dendritic spines. *Sci New York N Y*. **319**, 1683–7 (2008).
11. B. R. Kraemer, S. O. Yoon, B. D. Carter, The biological functions and signaling mechanisms of the p75 neurotrophin receptor. *Handb. Exp. Pharmacol*. **220**, 121–164 (2014).
12. L. Mou, B. G. Dias, H. Gosnell, K. J. Ressler, Gephyrin plays a key role in BDNF-dependent regulation of amygdala surface GABAARs. *Neuroscience* **255**, 33–44 (2013).
13. H. Wood, A role for double-negative T cells in post-stroke neuroinflammation. *Nat. Rev. Neurol*. **15**, 246–247 (2019).
14. K. M. Lenz, L. H. Nelson, Microglia and beyond: Innate immune cells as regulators of brain development and behavioral function. *Front. Immunol*. **9**, 698 (2018).
15. K. M. Lenz, B. M. Nugent, R. Haliyur, M. M. McCarthy, Microglia are essential to masculinization of brain and behavior. *J. Neurosci*. **33**, 2761–2772 (2013).
16. K. Reemst, S. C. Noctor, P. J. Lucassen, E. M. Hol, The indispensable roles of microglia and astrocytes during brain development. *Front. Hum. Neurosci*. **10**, 566 (2016).
17. S. Fumagalli, C. Perego, F. Ortolano, M.-G. D. Simoni, CX3CR1 deficiency induces an early protective inflammatory environment in ischemic mice. *Glia* **61**, 827–842 (2013).
18. Y. Li, X.-F. Du, C.-S. Liu, Z.-L. Wen, J.-L. Du, Reciprocal regulation between resting microglial dynamics and neuronal activity in vivo. *Dev. Cell* **23**, 1189–1202 (2012).
19. C. Cserép, B. Pósfai, N. Lénárt, R. Fekete, Z. I. László, Z. Lele, B. Orsolits, G. Molnár, S. Heindl, A. D. Schwarcz, K. Ujvári, Z. Környei, K. Tóth, E. Szabadits, B. Sperlágh, M. Baranyi, L. Csiba, T. Hortobágyi, Z. Maglóczky, B. Martinecz, G. Szabó, F. Erdélyi, R. Szipőcs, M. M. Tamkun, B. Gesierich, M. Duering, I. Katona, A. Liesz, G. Tamás, Á. Dénes,

20. Z. Chen, W. Jalabi, K. B. Shpargel, K. T. Farabaugh, R. Dutta, X. Yin, G. J. Kidd, C. C. Bergmann, S. A. Stohlman, B. D. Trapp, Lipopolysaccharide-induced microglial activation and neuroprotection against experimental brain injury is independent of hematogenous TLR4. *J Neurosci Official J Soc Neurosci*. **32**, 11706–11715 (2012).
21. S.-W. Jang, X. Liu, M. Yepes, K. R. Shepherd, G. W. Miller, Y. Liu, W. D. Wilson, G. Xiao, B. Blanchi, Y. E. Sun, K. Ye, A selective TrkB agonist with potent neurotrophic activities by 7,8-dihydroxyflavone. *P Natl Acad Sci Usa*. **107**, 2687–2692 (2010).
22. M. Bergeron, A. Y. Yu, K. E. Solway, G. L. Semenza, F. R. Sharp, Induction of hypoxia-inducible factor-1 (HIF-1) and its target genes following focal ischaemia in rat brain. *Eur. J. Neurosci*. **11**, 4159–4170 (1999).
23. S.-W. Lai, J.-H. Chen, H.-Y. Lin, Y.-S. Liu, C.-F. Tsai, P.-C. Chang, D.-Y. Lu, C. Lin, Regulatory effects of neuroinflammatory responses through brain-derived neurotrophic factor signaling in microglial cells. *Mol. Neurobiol*. **55**, 7487–7499 (2018).
24. Y. Béjot, A. Prigent-Tessier, C. Cachia, M. Giroud, C. Mossiat, N. Bertrand, P. Garnier, C. Marie, Time-dependent contribution of non neuronal cells to BDNF production after ischemic stroke in rats. *Neurochem. Int*. **58**, 102–111 (2010).
25. S. K. Tyagarajan, H. Ghosh, G. E. Yévenes, I. Nikonenko, C. Ebeling, C. Schwerdel, C. Sidler, H. U. Zeilhofer, B. Gerrits, D. Muller, J.-M. Fritschy, Regulation of GABAergic synapse formation and plasticity by GSK3beta-dependent phosphorylation of gephyrin. *Proc. Natl. Acad. Sci*. **108**, 379–384 (2011).
26. S. K. Tyagarajan, H. Ghosh, G. E. Yévenes, S. Y. Imanishi, H. U. Zeilhofer, B. Gerrits, J.-M. Fritschy, Extracellular signal-regulated kinase and glycogen synthase kinase 3β regulate gephyrin postsynaptic aggregation and GABAergic synaptic function in a calpain-dependent mechanism. *J. Biol. Chem*. **288**, 9634–9647 (2013).
27. G. P. Morris, A. L. Wright, R. P. Tan, A. Gladbach, L. M. Ittner, B. Vissel, A comparative study of variables influencing ischemic injury in the longa and koizumi methods of intraluminal filament middle cerebral artery occlusion in mice. *Plos One*. **11**, e0148503 (2016).
28. N. Yassi, L. Churilov, B. C. V. Campbell, G. Sharma, R. Bammer, P. M. Desmond, M. W. Parsons, G. W. Albers, G. A. Donnan, S. M. Davis, E. Investigators, D. Investigators, The association between lesion location and functional outcome after ischemic stroke. *Int. J. Stroke* **10**, 1270–1276 (2015).
29. L. Zhou, F. Li, H.-B. Xu, C.-X. Luo, H.-Y. Wu, M.-M. Zhu, W. Lu, X. Ji, Q.-G. Zhou, D.-Y. Zhu, Treatment of cerebral ischemia by disrupting ischemia-induced interaction of nNOS with PSD-95. *Nat. Med*. **16**, 1439–1443 (2010).
30. C. N. Parkhurst, G. Yang, I. Ninan, J. N. Savas, J. R. Yates, J. J. Lafaille, B. L. Hempstead, D. R. Littman, W.-B. Gan, Microglia promote learning-dependent synapse formation through brain-derived neurotrophic factor. *Cell* **155**, 1596–1609 (2013).
31. M. R. P. Elmore, L. A. Hohsfield, E. A. Kramár, L. Soreq, R. J. Lee, S. T. Pham, A. R. Najafi, E. E. Spangenberg, M. A. Wood, B. L. West, K. N. Green, Replacement of microglia in the aged brain reverses cognitive, synaptic, and neuronal deficits in mice. *Aging Cell* **17**, e12832 (2018).
32. E. E. Spangenberg, R. J. Lee, A. R. Najafi, R. A. Rice, M. R. P. Elmore, M. Blurton-Jones, B. L. West, K. N. Green, Eliminating microglia in Alzheimer's mice prevents neuronal loss without modulating amyloid-β pathology. *Brain J Neurology*. **139**, 1265–1281 (2016).
33. M. R. P. Elmore, A. R. Najafi, M. A. Koike, N. N. Dagher, E. E. Spangenberg, R. A. Rice, M. Kitazawa, B. Matusow, H. Nguyen, B. L. West, K. N. Green, Colony-stimulating factor 1 receptor signaling is necessary for microglia viability, unmasking a microglia progenitor cell in the adult brain. *Neuron* **82**, 380–397 (2014).
34. F. Calabrese, A. C. Rossetti, G. Racagni, P. Gass, M. A. Riva, R. Molteni, Brain-derived neurotrophic factor: A bridge between inflammation and neuroplasticity. *Front. Cell. Neurosci*. **8**, 430 (2014).
35. K. Inoue, M. Tsuda, Microglia in neuropathic pain: Cellular and molecular mechanisms and therapeutic potential. *Nat. Rev. Neurosci*. **19**, 138–152 (2018).
36. Y. Jiang, N. Wei, J. Zhu, T. Lu, Z. Chen, G. Xu, X. Liu, Effects of brain-derived neurotrophic factor on local inflammation in experimental stroke of rat. *Mediators Inflamm*. **2010**, 372423 (2010).
37. Z. Wei, S. Chigurupati, T. V. Arumugam, D.-G. Jo, H. Li, S. L. Chan, Notch activation enhances the microglia-mediated inflammatory response associated with focal cerebral ischemia. *Stroke* **42**, 2589–2594 (2011).
38. L. Buscemi, M. Price, P. Bezzi, L. Hirt, Spatio-temporal overview of neuroinflammation in an experimental mouse stroke model. *Sci Rep-uk*. **9**, 507 (2019).
39. R. C. Paolicelli, A. Jawaid, C. M. Henstridge, A. Valeri, M. Merlini, J. L. Robinson, E. B. Lee, J. Rose, S. Appel, V. M.-Y. Lee, J. Q. Trojanowski, T. Spires-Jones, P. E. Schulz, L. Rajendran, TDP-43 depletion in microglia promotes amyloid clearance but also induces synapse loss. *Neuron* **95**, 297-308.e6 (2017).
40. W. D. Rajan, B. Wojtas, B. Gielniewski, A. Gieryng, M. Zawadzka, B. Kaminska, Dissecting functional phenotypes of microglia and macrophages in the rat brain after transient cerebral ischemia. *Glia* **67**, 232–245 (2018).

Microglia monitor and protect neuronal function through specialized somatic purinergic junctions. *Sci New York N Y*. **367**, 528–537 (2019).

41. A. N. Clarkson, B. S. Huang, S. E. Macisaac, I. Mody, S. T. Carmichael, Reducing excessive GABA-mediated tonic inhibition promotes functional recovery after stroke. *Nature* **468**, 305–309 (2010).

42. B. Dejanovic, G. Schwarz, Neuronal nitric oxide synthase-dependent S-nitrosylation of gephyrin regulates gephyrin clustering at GABAergic synapses. *J. Neurosci.* **34**, 7763–7768 (2014).

43. H. S. Je, F. Yang, Y. Ji, S. Potluri, X.-Q. Fu, Z.-G. Luo, G. Nagappan, J. P. Chan, B. Hempstead, Y.-J. Son, B. Lu, ProBDNF and mature BDNF as punishment and reward signals for synapse elimination at mouse neuromuscular junctions. *J Neurosci Official J Soc Neurosci.* **33**, 9957–9962 (2013).

44. N. H. Woo, H. K. Teng, C.-J. Siao, C. Chiaruttini, P. T. Pang, T. A. Milner, B. L. Hempstead, B. Lu, Activation of p75NTR by proBDNF facilitates hippocampal long-term depression. *Nat. Neurosci.* **8**, 1069–1077 (2005).

45. D. R. Kaplan, F. D. Miller, Neurotrophin signal transduction in the nervous system. *Curr. Opin. Neurobiol.* **10**, 381–391 (2000).

46. P.-Y. Lin, E. T. Kavalali, L. M. Monteggia, Genetic dissection of presynaptic and postsynaptic bdnf-trkb signaling in synaptic efficacy of ca3-ca1 synapses. *Cell Rep.* **24**, 1550–1561 (2018).

47. J. N. Jovanovic, P. Thomas, J. T. Kittler, T. G. Smart, S. J. Moss, Brain-derived neurotrophic factor modulates fast synaptic inhibition by regulating GABA$_A$ receptor phosphorylation, activity, and cell-surface stability. *J. Neurosci.* **24**, 522–530 (2004).

48. I. Brünig, S. Penschuck, B. Berninger, J. A. Benson, J. M. Fritschy, BDNF reduces miniature inhibitory postsynaptic currents by rapid downregulation of GABAA receptor surface expression. *Eur. J. Neurosci.* **13**, 1320–1328 (2001).

49. F. Ferrini, Y. D. Koninck, Microglia control neuronal network excitability via BDNF signalling. *Neural Plast.* **2013**, 429815 (2013).

50. R. E. Sorge, J. C. S. Mapplebeck, S. Rosen, S. Beggs, S. Taves, J. K. Alexander, L. J. Martin, J.-S. Austin, S. G. Sotocinal, D. Chen, M. Yang, X. Q. Shi, H. Huang, N. J. Pillon, P. J. Bilan, Y. Tu, A. Klip, R.-R. Ji, J. Zhang, M. W. Salter, J. S. Mogil, Different immune cells mediate mechanical pain hypersensitivity in male and female mice. *Nat. Neurosci.* **18**, 1081–1083 (2015).

51. S. Beggs, T. Trang, M. W. Salter, P2X4R$^+$ microglia drive neuropathic pain. *Nat. Neurosci.* **15**, 1068–1073 (2012).

52. T. Masuda, S. Iwamoto, R. Yoshinaga, H. Tozaki-Saitoh, A. Nishiyama, T. W. Mak, T. Tamura, M. Tsuda, K. Inoue, Transcription factor IRF5 drives P2X4R$^+$-reactive microglia gating neuropathic pain. *Nat. Commun.* **5**, 3771 (2014).

53. Y. Gan, Q. Liu, W. Wu, J.-X. Yin, X.-F. Bai, R. Shen, Y. Wang, J. Chen, A. L. Cava, J. Poursine-Laurent, W. Yokoyama, F.-D. Shi, Ischemic neurons recruit natural killer cells that accelerate brain infarction. *P Natl Acad Sci Usa.* **111**, 2704–2709 (2014).

54. Z. Chen, W. Jalabi, W. Hu, H.-J. Park, J. T. Gale, G. J. Kidd, R. Bernatowicz, Z. C. Gossman, J. T. Chen, R. Dutta, B. D. Trapp, Microglial displacement of inhibitory synapses provides neuroprotection in the adult brain. *Nat. Commun.* **5**, 4486 (2014).

55. N. C. Guérineau, R. A. McKinney, D. Debanne, P. Mollard, B. H. Gähwiler, Organotypic cultures of the rat anterior pituitary: Morphology, physiology and cell-to-cell communication. *J Neurosci Meth.* **73**, 169–176 (1997).

56. C. E. Gee, P. Benquet, O. Raineteau, L. Rietschin, S. W. Kirbach, U. Gerber, NMDA receptors and the differential ischemic vulnerability of hippocampal neurons. *Eur. J. Neurosci.* **23**, 2595–2603 (2006).

57. S. Yona, K.-W. Kim, Y. Wolf, A. Mildner, D. Varol, M. Breker, D. Strauss-Ayali, S. Viukov, M. Guilliams, A. Misharin, D. A. Hume, H. Perlman, B. Malissen, E. Zelzer, S. Jung, Fate mapping reveals origins and dynamics of monocytes and tissue macrophages under homeostasis. *Immunity* **38**, 79–91 (2012).

58. M. Rios, G. Fan, C. Fekete, J. Kelly, B. Bates, R. Kuehn, R. M. Lechan, R. Jaenisch, Conditional deletion of brain-derived neurotrophic factor in the postnatal brain leads to obesity and hyperactivity. *Mol. Endocrinol.* **15**, 1748–1757 (2001).

59. M. Vaas, R. Ni, M. Rudin, A. Kipar, J. Klohs, Extracerebral tissue damage in the intraluminal filament mouse model of middle cerebral artery occlusion. *Front. Neurol.* **8**, 85 (2017).

60. T. Notter, P. Panzanelli, S. Pfister, D. Mircsof, J.-M. Fritschy, A protocol for concurrent high-quality immunohistochemical and biochemical analyses in adult mouse central nervous system. *Eur. J. Neurosci.* **39**, 165–175 (2014).

61. G. Weskamp, L. F. Reichardt, Evidence that biological activity of NGF is mediated through a novel subclass of high affinity receptors. *Neuron* **6**, 649–663 (1991).